BRNO UNIVERSITY OF TECHNOLOGY

FACULTY OF MECHANICAL ENGINEERING

FAKULTA STROJNÍHO INŽENÝRSTVÍ

INSTITUTE OF PHYSICAL ENGINEERING

ÚSTAV FYZIKÁLNÍHO INŽENÝRSTVÍ

NON-LINEAR IMAGING IN 100 KEV TRANSMISSION ELECTRON MICROSCOPY

NELINEÁRNÍ ZOBRAZENÍ V 100 KEV TRANSMISNÍM ELEKTRONOVÉM MIKROSKOPU

BACHELOR'S THESIS
BAKALÁŘSKÁ PRÁCE

AUTHOR   Michal Brzica
AUTOR PRÁCE

SUPERVISOR   Ing. Ondřej Sháněl, Ph.D.
VEDOUCÍ PRÁCE

Assignment Bachelor's Thesis

Institut:	Institute of Physical Engineering
Student:	**Michal Brzica**
Degree programm:	Physical Engineering and Nanotechnology
Branch:	no specialisation
Supervisor:	**Ing. Ondřej Sháněl, Ph.D.**
Academic year:	2022/23

As provided for by the Act No. 111/98 Coll. on higher education institutions and the BUT Study and Examination Regulations, the director of the Institute hereby assigns the following topic of Bachelor's Thesis:

Non–linear imaging in 100 keV transmission electron microscopy

Brief Description:

Cryo–transmission electron microscopy (TEM) has experienced a huge rise among biologists since the beginning of the 21st century, when it enabled the first large protein structures to be visualized at the atomic level.

Now the big trend is to make this technique cheaper so that most scientific laboratories can afford this technique. One option is to use 100 keV TEM systems due to their better affordability compared to larger, 200 and 300 keV systems.

However, to fully understand the imaging at 100 keV, it is necessary to understand the contrast transfer function (CTF), including its non–linear part, which has been neglected for systems with higher accelerating voltages.

Bachelor's Thesis goals:

1. Comparison of CTFs for 100, 200 and 300 keV systems.
2. Derivation of the CTF including its non–linear components.
3. Study of the CTF for a 100 keV system focusing on the comparison of the CTF with only linear terms and with non–linear and linear terms.

Recommended bibliography:

HAWKES, P. W. a E. KASPER. Principles of electron optics. Second edition. London: Academic Press, 2018. ISBN 0081022565.

ORLOFF, J. Handbook of charged particle optics. 2nd ed. Boca Raton: CRC Press/Taylor & Francis, 2009. ISBN 978-1-4200-4554-3.

Deadline for submission Bachelor's Thesis is given by the Schedule of the Academic year2022/23

In Brno,

L. S.

_____   _____

prof. RNDr. Tomáš Šikola, CSc.   doc. Ing. Jiří Hlinka, Ph.D.
Director of the Institute   FME dean

Abstrakt
Bakalářská práce se zabývá popisem zobrazení v transmisním elektronovém mikroskopu. Práce je zaměřena na odvození rovnice popisující pozorovanou intenzitu a kontrast v rovině detektoru. V práci jsou porovnány teoretické lineární a nelineární rovnice zobrazení pro výsledný kontrast s reálnými daty při urychlovacích napětí 100, 200 a 300 kV. Vliv jednotlivých nelineárních členů na pozorované rozlišení je diskutován.

Summary
The bachelor thesis deals with the description of imaging in a transmission electron microscope. The thesis is mainly focused on the derivation of the equation describing the observed intensity in the detector plane. A comparison of the form of the linear and non-linear equations for the observed intensity is followed by a comparison of the derived theory with photographed samples at different accelerating voltages. The effect of the individual non-linear terms on the observed resolution is then determined.

Klíčová slova
TEM, zobrazovací teorie, 100 kV, 200 kV, 300 kV, lineární zobrazování, nelineární zobrazování.

Keywords
TEM, imaging theory, 100 kV, 200 kV, 300 kV, linear imaging, non-linear imaging

I declare that I wrote the bachelor's thesis titled "Non-linear imaging in 100 keV transmission electron microscopy" independently, under the guidance of the advisor and using exclusively the technical references and other sources of information cited in the thesis and listed in the comprehensive bibliography at the end of the thesis.

Michal Brzica

Contents

1. Introduction

Electron microscopy, unlike conventional light microscopy, uses electrons as an illumination source. The most significant advantage is that it can achieve several orders of magnitude higher resolution than conventional light microscopy. Transmission electron microscopy primarily examines those electrons that pass through the sample under examination. The history of electron microscopy and the study of electrons themselves dates back to the late 19th and early 20th century.

In 1897, Sir Joseph John Thomson discovered a negatively charged particle during a cathode ray experiment. Furthermore, he was able to demonstrate that the trajectory of these particles could be altered by an external magnetic or electric field [1].

In 1924, Louis de Broglie postulated that every object had its own wavelength. This discovery led to the idea of using electrons instead of photons for imaging objects [2].

Two years later, Hans Busch proposed a device - a solenoid. The field of this device would curve the trajectory of electrons in a similar way as glass lenses focus light rays. Eventually, this type of lens would be used in a new type of microscope - the electron microscope [3].

Thirty years after the discovery of the electron as a particle, George Paget Thomson showed that an electron can be considered a wave. He based his hypothesis on Louis De Broglie´s theory. Thomson proved this in an electron diffraction experiment on layers of various materials such as metals (aluminum and gold) and celluloid [4].

In 1931, Max Knoll and Ernst Ruska built the first transmission electron microscope. The total magnification of the instrument was only about 17.4x. The crucial point of this demonstration was the possibility of making a functional microscope where electrons act as the source of illumination [5].

Two years later, they created a system with a magnification of about 12,000x, which at the time exceeded the magnification capabilities of light microscopes tenfold [5].

The development of electron microscopy has continued with an increasing speed ever since. In 2021, imaging the specimen of $PrScO_3$ showed less than 20 pm resolution. The physical limitation of resolution at this level was mainly caused by the thermal fluctuations of the atoms themselves [6].

Main part of this bachelor thesis is organized into five chapters, which are summarized in the conclusion.

The chapter TEM Construction will describe the design of the transmission electron microscope, where the individual components and their basic principle will be discussed. The following chapter describes the single particle analysis method (SPA), which allows us to study proteins down to the atomic level. In the chapter TEM Imaging Theory, the imaging equation for the electron wave after interaction with the sample and passage through the lens system will be derived. After calculating the intensity of a given wave, the focus will be mainly on the higher-order terms. The chapter Non-linear Imaging will focus on an introduction to the effect of these non-linear terms on the observed resolution for a system with a lower accelerating voltage and potential impact in the scientific community. In the last section, the derived theory will be compared with measured data to confirm or disprove the influence of these non-linear terms on the observed resolution.

The images taken for this thesis were acquired on Tundra, Glacios, and Krios electron microscopes, and the graphs were plotted in the programming language Python.
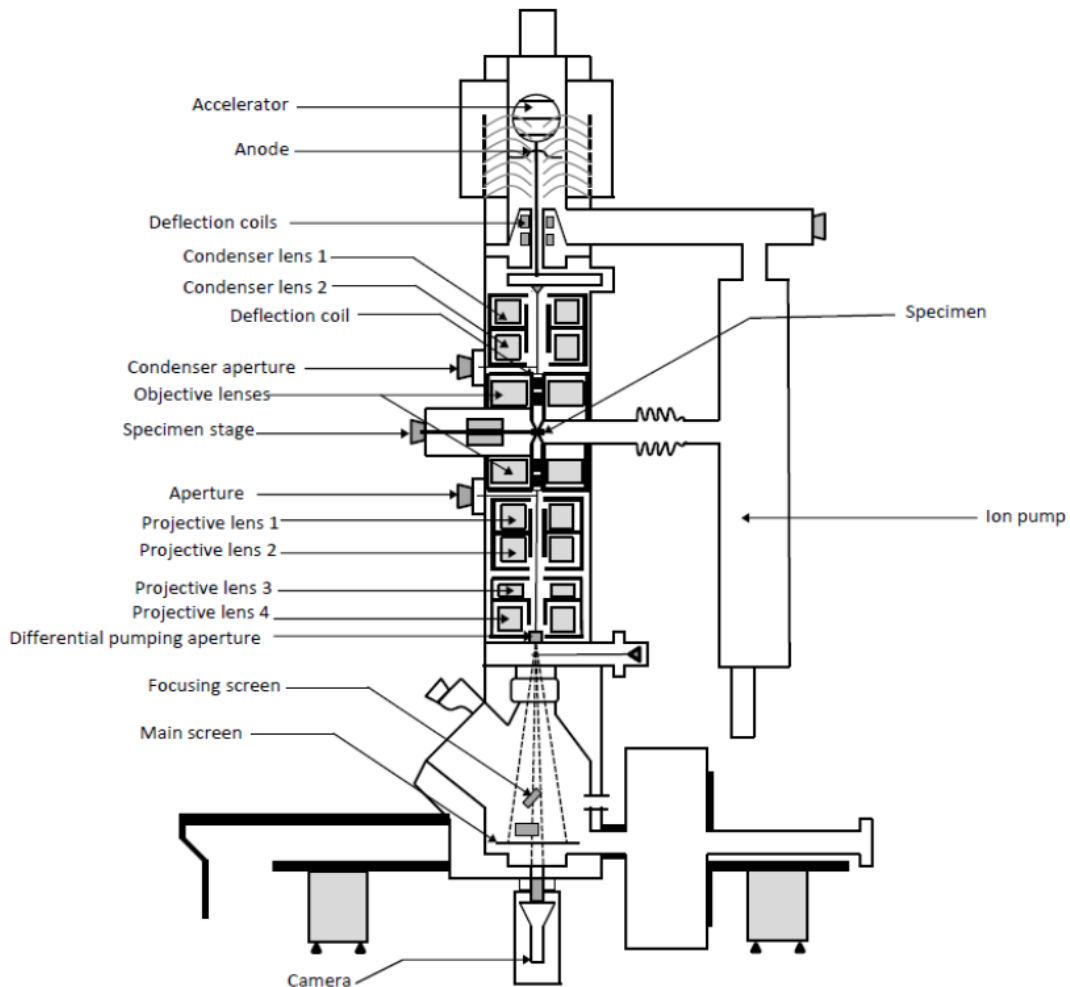
2. TEM Construction

Figure 2.1: Transmission electron microscope, adapted from [7].

A transmission electron microscope (TEM) produces a magnified image from electrons that pass through the sample; a simplified scheme of such a microscope is shown in Fig. 2.1.

In general, the instrument can be divided into 5 main modules [8]. Here is a brief summary of each module and its primary functions:

1. **Electron gun + accelerator** - The main function is to generate an electron beam using an electron source (gun) and accelerate it to a desired speed with high electrical potential. There are 3 main types of electron sources:

   (a) **Thermionic source** uses a tungsten (W) filament or a lanthanum hexaboride (LaB$_6$) crystal as a source of electrons. Once the current passing through the filament/crystal heats it up to a high enough temperature (around 2,700 K for tungsten and 1,700 K for lanthanum hexaboride [8]), the thermionic effect is exploited to overcome the Fermi level to generate an electron beam. The tungsten thermionic source has slightly worse properties in terms of current density, energy spread, or lifespan than its counterpart. Therefore a crystal of LaB$_6$ with $\langle 110 \rangle$ orientation is mainly used as the preferred source [8].

3

(b) **Cold field emission gun (CFEG)** uses a strong electric field between the filament and the extraction plate. This enables the electron to tunnel through the potential barrier and break away from the filament. The material used for such filament is tungsten with $\langle 310 \rangle$ orientation. CFEG has the best properties of all the electron sources. However, the limiting factors for a field-wide use are the maintenance of a 10^{-9} Pa vacuum conditions as well as financial inaccessibility.

(c) **Schottky field emission gun (SFEG)** combines a principle of the two sources mentioned above. A tunneling effect is reached by the combination of heating of the filament, assisted by an external electric field. In addition, the filament of W with $\langle 100 \rangle$ orientation is coated with ZrO_2 on the surface in order to improve the properties of the source, e.g., to lower the work function of the electrons [9].

2. **Condenser system** - The combination of condenser lenses and apertures (fixed and variable) is responsible for transferring electrons from the source to the sample. It typically consists of 2 or 3 lenses. The beam current arriving at the sample is controlled by the combination of changes in the first condenser lens excitation and the diameter of its aperture.

   The second condenser lens is used to set up an illuminated area size and a convergent angle in combination with a limiting aperture.

   The third condenser lens is used in combination with the second condenser lens to make the setup of the illuminated area and convergent angle independently manageable.

   Parallel beam illumination is a necessity during TEM imaging or TEM diffraction.

   In other applications, such as Scanning transmission electron microscopy (STEM) or during instrument alignments, the focus mode is preferred as it provides the smallest illuminated area on a sample.

   The optional third condenser lens provides flexibility in the setup of the illuminated area and its convergent angle.

3. **Objective lens + stage (specimen)** - It is responsible for creating the initial image, which is then magnified by other lenses. The manufacturing quality of an objective lens is crucial, as its magnification potential is the highest of all lenses (30 - 50 times).

   The specimen is usually in the middle of the objective lens on a sample holder. The requirements for the sample size and also for the preparation of the sample are critical, as discussed in the next chapter. The sample must be extremely thin, in general < 100 nm for imaging, for high-resolution TEM, the thickness must ideally be < 20 nm [8].

4. **Projector system** - Projector lenses are used to transfer the electrons to the detector and provide the final magnification of the image. Diffraction or imaging mode can be selected by varied excitation of the first projector lens. Subsequently, the following projector lenses will magnify the result on the detector. Four projector lenses are typically used to provide a rotation-free image.

5. **Image detection** - The last module in the electron microscope is utilized to detect the magnified image or the diffraction pattern of the sample. In modern electron microscopes, there are multiple types of devices capable of detecting electrons:

    (a) **Fluorescent screen** consists of small particles of ZnS, which emit light when an electron hits the screen. Simultaneously, a camera is pointed at the screen, so it is possible to observe the sample on the computer in real-time. This type of detection is helpful for easy orientation on the sample and initial sample description, as well as proper alignment of the system.

    (b) **Scintillation-based camera** is the main camera for TEM imaging. It consists of a scintillation layer which converts the electrons into photons. Optical fibers then transfer the newly generated photons toward the chip. The signal is then converted from an analogue signal to a digital signal.

    (c) **The direct-detection electron** camera is capable of detecting every single electron that hits the surface. It provides the best signal-to-noise ratio and the best resolution, but has several drawbacks. One of them is the cost of the camera, which is several times more expensive than the scintillation-based camera. Another disadvantage is poor radiation hardness and low dynamic range.

In addition to cameras, there are also detectors that separate the electrons according to the angle at which they arrive. This approach is used in scanning transmission electron microscopy. In general, there are 3 types of detectors:

    (a) **Bright field detector** - This detector provides information about electrons that have not been scattered at all or at a very small angle. This detector is useful for determining sample thickness.

    (b) **Annular dark-field detector** - Electrons scattered at higher angles are detected on the annular dark-field detector and provide information about the crystal structure of the sample. This type of detection is employed for the analysis of crystalline samples.

    (c) **High-angle annual dark-field detector** - The most scattered electrons give us information about the elements of the examined sample. Elements with a higher atomic number scatter electrons more, creating a so-called Z-contrast.

There are other optical elements in TEM - apertures, deflectors, and stigmators.

1. The main function of an aperture is to block electrons traveling at too wide convergence angles or to limit the beam current reaching the specimen, e.g., in order to mitigate the specimen damage.

2. Deflectors are two pairs of magnetic or electrostatic/dynamic coils. Their main function is to optimize the path of electrons that travel from one module to the other. In reality, the modules are not perfectly mechanically aligned, so the electron trajectory must be adjusted to minimize the effect of aberrations. There are two pairs of coils to correct the shift and the tilt of the beam individually. There are usually 3 deflectors in a TEM - gun deflectors, beam deflectors, and image deflectors.

3. Stigmators are multipoles used to correct n-fold astigmatism. Their primary purpose is to correct beam/image astigmatism. Astigmatism is caused by lens imperfections. Commonly 2- and 3-fold stigmators are used within the electron microscopes.

The instrument must be evacuated due to the filament and specimen contamination risk caused by gases, particularly H_2O, N_2, O_2, CO and H_2 [9]. Additionally, any contaminants present in the column disrupt the electron beam traveling through, resulting in scattering noise. Each of the aforementioned modules of the microscope requires different level of vacuum for optimal operation. A combination of multiple vacuum pump types is used to achieve the required vacuum level.

1. Mechanical (rotary) pump provides the rough vacuum in the range of $\approx 10^{-1}$ Pa. It is the first pump that allows the pressure to be reduced enough to allow other pumps to operate efficiently.

2. Turbomolecular pump consists of two main parts - moving and stationary blades. The combination of moving and stationary parts provides the best possible path for air particles to escape. After the molecule is attached to the moving blade, it is blasted away after a certain period of time with the help of the energy supplied by the rotational motion. The stationary blades are used to deflect the molecules.

3. Ion getter pump is the vacuum pump creating the level of vacuum in the range of $10^{-4} - 10^{-8}$ Pa. It captures particles by ionization caused by an external high voltage at the cathodes and captures them by chemisorption into the anode.

4. Cryogenic pump works by cooling the microscope column typically with liquid nitrogen, which is contained in a dewar attached to the microscope. If a molecule reaches the surface, its kinetic energy is reduced to a level where it no longer has enough energy to escape.

5. Nonevaporable getter pump improves the level of vacuum by capturing the particles of active gases inside the material [10] . By implementation of another type of pump, the level of vacuum can be enhanced in areas of the microscope where the need for ultra-high vacuum is crucial, e.g., electron gun.

3. Single Particle Analysis and Basic Principles

Before the rise of electron microscopy, the structure of molecules and biological samples was mostly studied by X-ray crystallography and nuclear magnetic resonance. However, cryo-electron microscopy is becoming increasingly popular nowadays, see as shown in Fig. 3.1. One of the reasons is the possible achievable resolution of individual proteins caused by the overall technology development, especially in the areas of electron sources and cameras. There are major advantages in comparison to X-ray crystallography. Scientists can observe proteins in their natural hydrated forms without forcing them into forming crystals. Furthermore, a comparatively small amount of sample is needed for a comprehensive analysis [11].
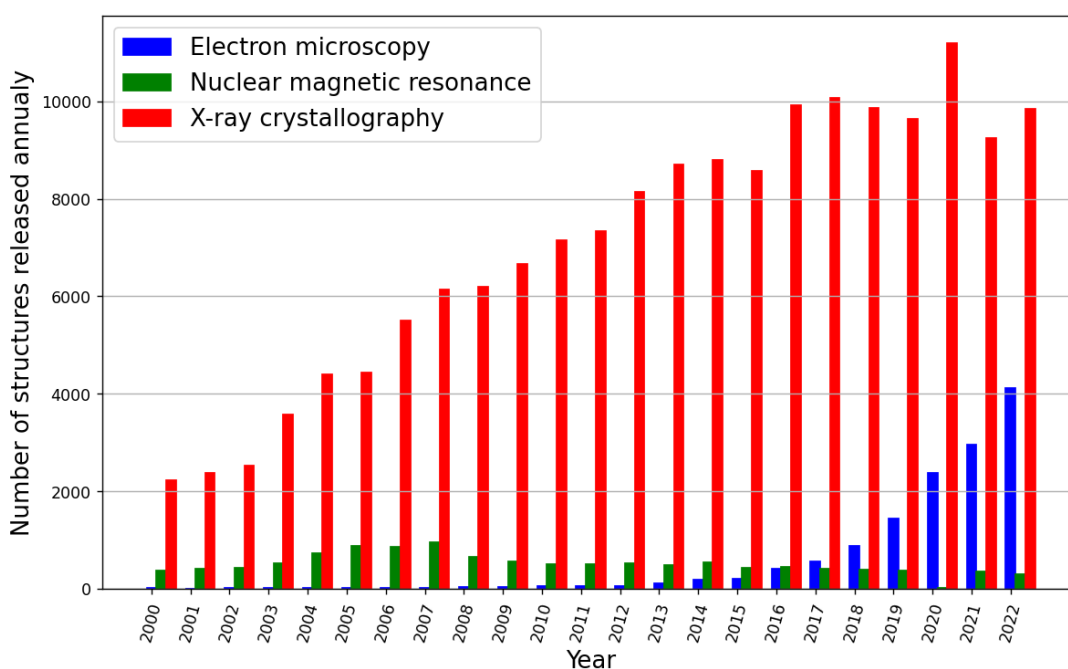

Figure 3.1: Growth of released structures - proteins per year. Data taken from [12].

Single particle analysis (SPA) is based on imaging hundreds of thousands of the identical particles fixed in vitreous ice and imaged by electron microscopy. The greatest contribution to the development of single particle analysis and cryo-electron microscopy (cryoEM) was made by Joachim Frank, Richard Henderson, and Jacques Dubochet. They were honored with the Nobel Prize in chemistry in 2017 [13].

There were several techniques that had to be mastered in order to produce life-like reconstructions of the studied molecules. These techniques can be divided into three categories, which are described in the following sections 3.1, 3.2 and 3.3 [14].

Today record in SPA is ≈ 1.2 Å at Krios 300 kV [15]. However, 300 kV systems are not affordable for a wide biological community, and so 100 kV systems are developed to start the age of broad SPA.

3.1. Specimen Preparation

The specimen cooling process is an important stepping stone in the cryoEM process. If the sample is not frozen fast enough, the aqueous solution will form crystals which obstruct the electron beam as well as damage the sample.

Therefore, it was necessary to devise a method capable of freezing the sample quickly enough, namely in order of 10^5 K/s [16]. At this rate, the aqueous phase of the buffer does not have enough time to arrange its molecules into crystals. This method used for preparing samples in cryoEM is called vitrification.

The purity, concentration, aggregation propensity, as well as chemical and thermal stability of the protein solution, must be ensured prior to vitrification.

The choice of the sample carrier also has an impact on the success of the experiment. These carriers, also termed grids, consist of a metal net covered by a thin carbon membrane. A few examples of materials used for grid manufacturing are copper, gold, and molybdenum. Copper grids are the most common, but golden grids are more suitable for certain specialised purposes, e.g., culturing cells on the grid.

Following the application of a liquid sample on the grid of choice, the excess liquid is blotted away. The sample is then immersed into a container with liquid ethane [17]. This approach to vitrification is named the plunge freezing method, shown in Fig. 3.2.

3.2. Cryo-electron Microscopy

Following the vitrification process, the sample must remain at liquid nitrogen temperature at all times to keep the vitreous ice structure. The sample area of the electron microscope therefore must be cooled down to liquid nitrogen temperature for imaging vitrified biological samples.

Furthermore, ensuring a low beam dose rate is essential due to the inevitable damage caused by the electron impact.

Additionally, a sufficient spatial coherence of an electron source is crucial for imaging the sample in an electron microscope. Spatial and temporal coherence have the greatest influence on the damping envelope function in the contrast transfer function. Each of these two components will be described in more detail in the following chapter, which covers transmission electron microscope imaging.

To achieve better resolution, spatial coherence was improved by implementing a field emission electron gun. This ensures not only better spatial resolution, but also higher brightness and longer lifetime [14].

When it comes to imaging a biological sample, one of the most critical parameters is contrast. Biological samples are mostly composed of atoms with low proton number (C, N, O, H), and their electron interaction is relatively weak compared to atoms with higher proton number (Au, Ag, Fe,...). This produces low-contrast images and an inferior signal-to-noise ratio [13].

The main solution for increasing contrast of biological samples is imaging in underfocus or implementation of some kind of a phase plate.
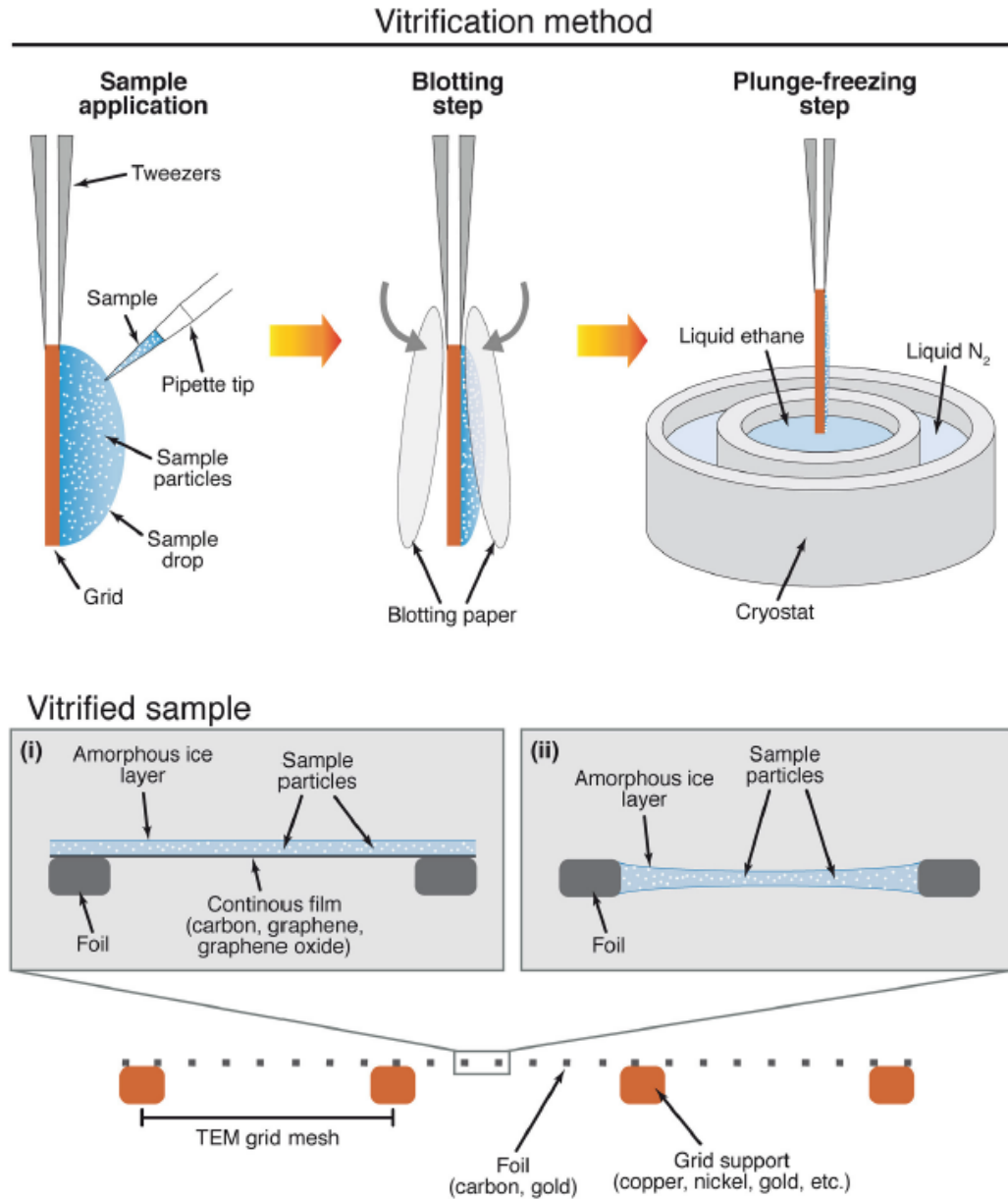
Figure 3.2: Plunge freezing method, adapted from [17].

3.3. Mathematical/Computational Approaches

The principle of single particle analysis lies in utilizing methods capable of creating a 3D image model of a particle from 1000+ 2D images obtained from a microscope. One of the first pieces of software to do this was SPIDER, created by Joachim Frank and his coworkers [14].

The procedure from micrograph collection to the 3D model can be seen in Fig. 3.3. First, a sufficient number of micrographs of a given biological molecule in all orientations must be acquired. As time passes during the imaging process, the samples are being increasingly damaged by the electron beam radiation. Furthermore, melting of the ice causes the drift of the imaged sample. As a result of these events, it is important to
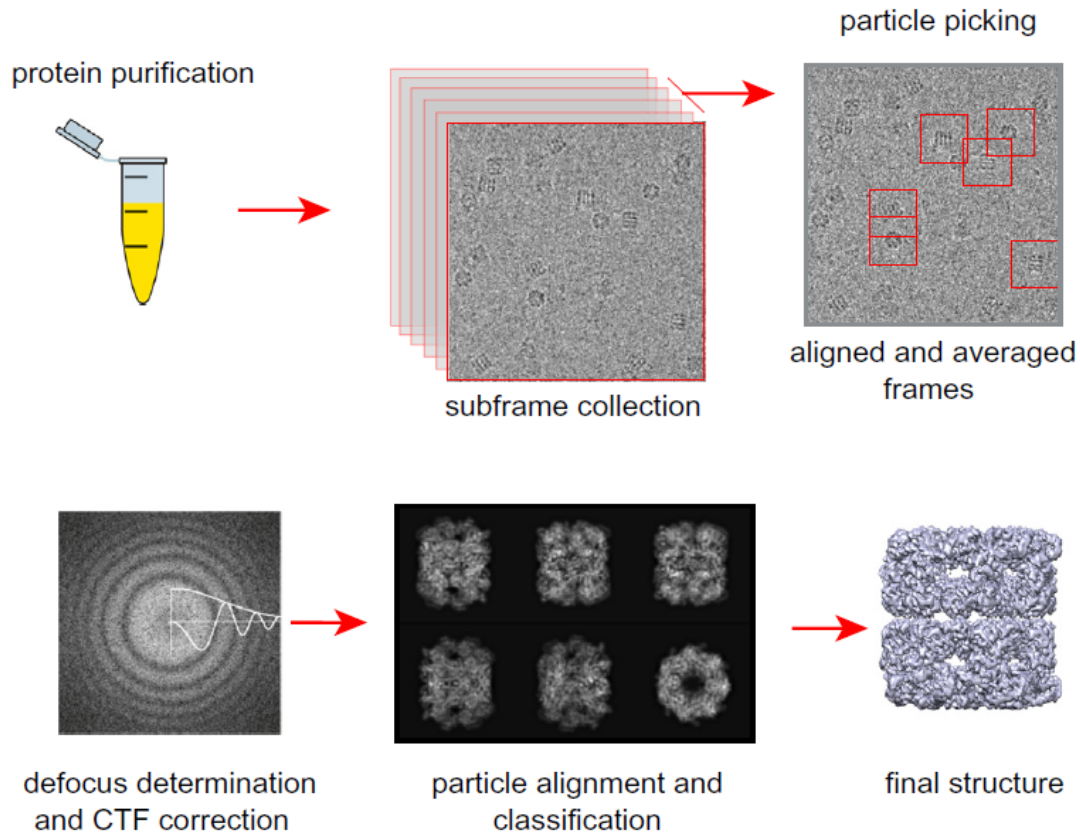
Figure 3.3: SPA workflow, adapted from [18].

align the movie frames (set of multiple images of the same area) via motion correction algorithms to suppress image drift.

After the correction of motion on the averaged image from all frames, it is possible to make the first contrast transfer function (CTF) estimation. When the CTF estimation and correction are done, the particles of sufficient quality must be picked. Although this process is automated, it may result in a selection of images that contain unwanted particles, such as impurities. An expertise in structural biology is often required for this phase of the analysis. Once all these steps have been carried out, we can move on to the actual 3D reconstruction of the studied particle [18].

4. TEM Imaging Theory

4.1. Derivation of Wave Intensity

In order to derive the image intensity, we need to make several assumptions. The first is that the sample consists of only few layers of atoms and multiscattering is not present. Another simplification is that the incident wave is perfectly parallel and normalized to one.
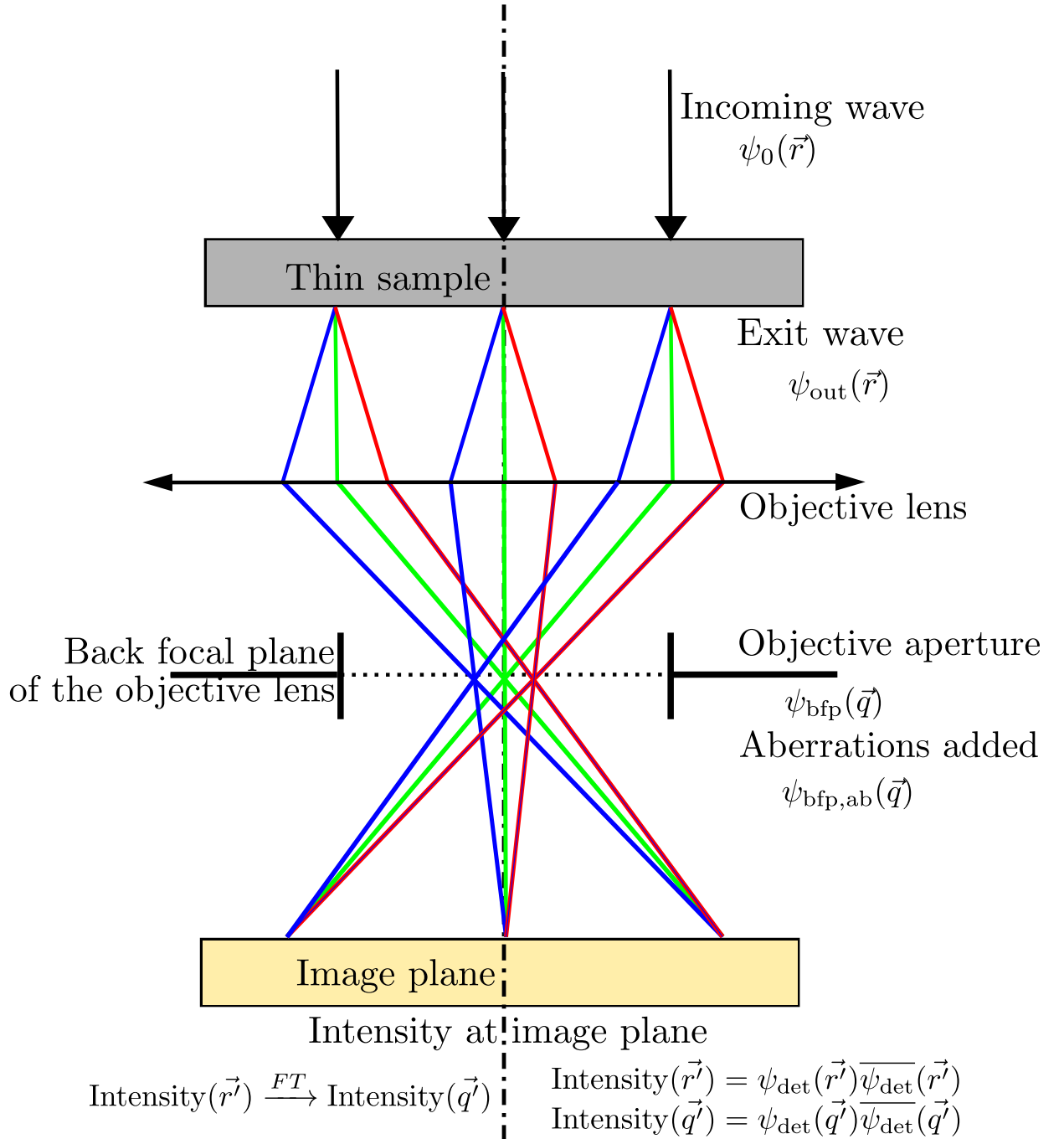

Figure 4.1: Schematic of the electron beam transmission through the sample and the imaging on the camera. Adapted from [19].

4.1. DERIVATION OF WAVE INTENSITY

Once these approximations are established, a description of TEM imaging can be made as follows:

Parallel illumination is considered, so an incident wave at the sample can be simply written as:

$$\psi_0(\vec{r}) = 1, \tag{4.1}$$

when intensity is normalized to 1. The wave arising after passing through the sample can be written as:

$$\begin{aligned}\psi_{\text{out}}(\vec{r}) &= A(\vec{r})\psi_0(\vec{r})e^{i\varphi(\vec{r})} \\ &= e^{\epsilon(\vec{r})}\psi_0(\vec{r})e^{i\varphi(\vec{r})},\end{aligned} \tag{4.2}$$

where $\epsilon(\vec{r}) = \ln[A(\vec{r})]$ is the amplitude object function, $\vec{r}$ represents coordinate at the specimen plane, and $\varphi(\vec{r})$ is the phase object function.

Assuming $\psi_0(\vec{r}) = 1$, then Eq. 4.2 can be rewritten as:

$$\begin{aligned}\psi_{\text{out}}(\vec{r}) &= A(\vec{r})e^{i\varphi(\vec{r})} \\ &= e^{\epsilon(\vec{r})+i\varphi(\vec{r})}.\end{aligned} \tag{4.3}$$

Then we can expand the term into the Taylor series:

$$\psi_{\text{out}}(\vec{r}) = 1 + \epsilon(\vec{r}) + i\varphi(\vec{r}) + \frac{1}{2}[\epsilon(\vec{r}) + i\varphi(\vec{r})]^2 + \frac{1}{6}[\epsilon(\vec{r}) + i\varphi(\vec{r})]^3 + \dots \tag{4.4}$$

Assuming $\epsilon(\vec{r})$ and $\varphi(\vec{r}) \ll 1$, which is possible for thin samples (≤ 5 nm), we can take into consideration only the first terms and neglect the higher-order terms:

$$\psi_{\text{out}}(\vec{r}) = 1 + \epsilon(\vec{r}) + i\varphi(\vec{r}). \tag{4.5}$$

The wave ψ_{bfp} represents the Fourier transform of the wave emerging from the sample in the back focal plane of the objective lens:

$$\begin{aligned}\psi_{\text{bfp}}(\vec{q}) &= \text{FT}\{\psi_{\text{out}}\} \\ &= \delta(\vec{q}) + E(\vec{q}) + i\Phi(\vec{q}),\end{aligned} \tag{4.6}$$

where $\vec{q} = (q_x, q_y)$ represents the reciprocal coordinate at the back focal plane of the lens, $E(\vec{q})$ represents the Fourier transform of $\epsilon(\vec{r})$, and $\Phi(\vec{q})$ represents the Fourier transform of $\varphi(\vec{r})$.

In this thesis, Krivanek´s notation [20] will be used for the aberration function, and other formulas will also be used from [20] and [19]:

$$\chi(\vec{\theta}, \phi) = \sum_n \sum_m \frac{1}{n+1} \{C_{\text{n,m,a}}\vec{\theta}^{\text{n}+1} \cos(\text{m}\phi) + C_{\text{n,m,b}}\vec{\theta}^{\text{n}+1} \sin(\text{m}\phi)\}, \tag{4.7}$$

where n represents the order of the aberration, m is its multiplicity, $C_{\text{n,m,a}}$ and $C_{\text{n,m,b}}$ are aberrations coefficients at specimen plane, $\vec{\theta}(\vec{q})$ is the angle of deviation of electrons from the optical axis and ϕ is the azimuthal angle of the electron beam. $C_{\text{n,m,a}}$ describes mirror-symmetric aberrations and $C_{\text{n,m,b}}$ describes antisymmetric aberrations.

If the scattering angle $\vec{\theta}$ is small enough, we can make another approximation $\sin\theta \approx \theta$. After this simplification, the vector $\vec{q}$ can be written as:

12

$$\vec{q} = \frac{\vec{\theta}}{\lambda}. \tag{4.8}$$

The aberration function is written in terms of reciprocal coordinates and azimuthal angle as:

$$\chi(\vec{q}, \phi) = \sum_n \sum_m \frac{1}{n+1} \mathrm{Re}\{\mathbf{C}_{\mathrm{n,m}} \lambda^{\mathrm{n}+1} \vec{q}^{\mathrm{n}+1} \mathrm{e}^{-\mathrm{im}\phi}\}, \tag{4.9}$$

where $\mathbf{C}_{\mathrm{n,m}} = C_{\mathrm{n,m,a}} + \mathrm{i}C_{\mathrm{n,m,b}}$ are aberration coefficients at specimen plane.

For our calculations, we will assume two aberrations: defocus $(C_{1,0})$ and spherical aberration $(C_{3,0})$. Both of them are spherically symmetric. Other aberrations are not considered due to its lower impact to $\chi(\vec{q})$ for $C_{3,0}$ non-corrected TEM system.

This implies that our aberration polynomial can be written as:

$$\chi(\vec{q}) = \frac{1}{2}C_{1,0}\lambda^2\vec{q}^2 + \frac{1}{4}C_{3,0}\lambda^4\vec{q}^4. \tag{4.10}$$

Magnification is assumed as 1 for simplification. These aberrations are applied to the final image through lenses via the transfer function:

$$t_{\mathrm{L}}(\vec{q}) = \exp\left(-\frac{2\pi\mathrm{i}}{\lambda}\chi(\vec{q})\right). \tag{4.11}$$

To make further derivation more straightforward, we introduce a new variable $W(\vec{q})$, which can be written as:

$$W(\vec{q}) = \frac{2\pi}{\lambda}\chi(\vec{q}). \tag{4.12}$$

Wave at the objective lens back focal plane with aberrations can be described by using the equations Eq. 4.6, Eq. 4.11 and Eq. 4.12 as:

$$\psi_{\mathrm{bfp,ab}}(\vec{q}) = \delta(\vec{q}) + E(\vec{q})\mathrm{e}^{-\mathrm{i}W(\vec{q})} + \mathrm{i}\Phi(\vec{q})\mathrm{e}^{-\mathrm{i}W(\vec{q})}, \tag{4.13}$$

where we use the property of Dirac delta function $\delta(\vec{q}) \cdot \mathrm{e}^{-\mathrm{i}W(\vec{q})} = \delta(\vec{q})$.

We can divide $W(\vec{q})$ into two terms:

$$W(\vec{q}) = W_e(\vec{q}) + W_o(\vec{q}), \tag{4.14}$$

where $W_e(\vec{q})$ represents the even order terms and $W_o(\vec{q})$ represents the odd order terms.

In the next step, we consider $W(\vec{q}) = W_e(\vec{q}) + W_o(\vec{q})$ as $W = W_e + W_o$. Using Euler´s formula, we can rewrite the exponent into the function of cos and sin:

$$\mathrm{e}^{-\mathrm{i}W} = \mathrm{e}^{-\mathrm{i}(W_e + W_o)} = \cos(W_e + W_o) - \mathrm{i}\sin(W_e + W_o). \tag{4.15}$$

Using the trigonometric formulas for sin and cos, we can rewrite each term so the argument of each function contains only W_e or W_o:

$$\begin{aligned} \mathrm{e}^{-\mathrm{i}W} &= \cos(W_e)\cos(W_o) - \sin(W_e)\sin(W_o) \\ &\quad - \mathrm{i}\sin(W_e)\cos(W_o) - \mathrm{i}\cos(W_e)\sin(W_o). \end{aligned} \tag{4.16}$$

4.1. DERIVATION OF WAVE INTENSITY

If we rearrange the order of the terms, we might recognize another possible simplification:

$$
\begin{aligned}
\mathrm{e}^{-\mathrm{i}W} &= \cos(W_e)\cos(W_o) - \mathrm{i}\cos(W_e)\sin(W_o) \\
&\quad - \mathrm{i}[\sin(W_e)\cos(W_o) - \mathrm{i}\sin(W_e)\sin(W_o)] \\
&= \cos(W_e)\mathrm{e}^{-\mathrm{i}W_o} - \mathrm{i}\sin(W_e)\mathrm{e}^{-\mathrm{i}W_o}.
\end{aligned}
\tag{4.17}
$$

Now we can separate the inverse Fourier transform into two terms, each of them is represented by a goniometric function:

$$
\mathrm{IFT}\{\mathrm{e}^{-\mathrm{i}W(\vec{q})}\} = \mathrm{IFT}\{\cos[W_e(\vec{q})]\mathrm{e}^{-\mathrm{i}W_o(\vec{q})}\} - \mathrm{i}\,\mathrm{IFT}\{\sin[W_e(\vec{q})]\mathrm{e}^{-\mathrm{i}W_o(\vec{q})}\}.
\tag{4.18}
$$

To derive wave $\psi_{\mathrm{det}}(\vec{q'})$ at the detector plane with aberrations, we need to calculate the IFT of Eq. 4.13 as follows:

$$
\psi_{\mathrm{det}}(\vec{r'}) = \mathrm{IFT}\{\delta(\vec{q'}) + E(\vec{q'})\mathrm{e}^{-\mathrm{i}W(\vec{q'})} + \mathrm{i}\Phi(\vec{q'})\mathrm{e}^{-\mathrm{i}W(\vec{q'})}\},
\tag{4.19}
$$

where $\vec{q'} = \frac{\vec{q}}{M}$, where M represents the magnification, and $\vec{r'} = M\vec{r}$, and in $W(\vec{q'})$ the aberration coefficients are $C_{n,m,\mathrm{det}} = M^{n+1}C_{n,m,\mathrm{sample}}$.

Then we get the wave at the detector in real space coordinates:

$$
\psi_{\mathrm{det}}(\vec{r'}) = 1 + \epsilon(\vec{r'}) \otimes \mathrm{IFT}\{\mathrm{e}^{-\mathrm{i}W(\vec{q'})}\} + \mathrm{i}\varphi(\vec{r'}) \otimes \mathrm{IFT}\{\mathrm{e}^{-\mathrm{i}W(\vec{q'})}\},
\tag{4.20}
$$

where the symbol $\otimes$ represents the convolution of two functions.

As a final step in deriving the wave at the detector, we introduce Eq. 4.17 into Eq. 4.20. Then we obtain the complete formula for wave $\psi_{\mathrm{det}}(\vec{r'})$ and complex conjugate $\overline{\psi_{\mathrm{det}}}(\vec{r'})$ in the following formula:

$$
\begin{aligned}
\psi_{\mathrm{det}}(\vec{r'}) &= 1 + \epsilon(\vec{r'}) \otimes \mathrm{IFT}\{\cos[W_e(\vec{q'})]\mathrm{e}^{-\mathrm{i}W_o(\vec{q'})}\} + \varphi(\vec{r'}) \otimes \mathrm{IFT}\{\sin[W_e(\vec{q'})]\mathrm{e}^{-\mathrm{i}W_o(\vec{q'})}\} \\
&\quad - \mathrm{i}\epsilon(\vec{r'}) \otimes \mathrm{IFT}\{\sin[W_e(\vec{q'})]\mathrm{e}^{-\mathrm{i}W_o(\vec{q'})}\} + \mathrm{i}\varphi(\vec{r'}) \otimes \mathrm{IFT}\{\cos[W_e(\vec{q'})]\mathrm{e}^{-\mathrm{i}W_o(\vec{q'})}\},
\end{aligned}
\tag{4.21}
$$

$$
\begin{aligned}
\overline{\psi_{\mathrm{det}}}(\vec{r'}) &= 1 + \epsilon(\vec{r'}) \otimes \mathrm{IFT}\{\cos[W_e(\vec{q'})]\mathrm{e}^{+\mathrm{i}W_o(\vec{q'})}\} + \varphi(\vec{r'}) \otimes \mathrm{IFT}\{\sin[W_e(\vec{q'})]\mathrm{e}^{+\mathrm{i}W_o(\vec{q'})}\} \\
&\quad + \mathrm{i}\epsilon(\vec{r'}) \otimes \mathrm{IFT}\{\sin[W_e(\vec{q'})]\mathrm{e}^{+\mathrm{i}W_o(\vec{q'})}\} - \mathrm{i}\varphi(\vec{r'}) \otimes \mathrm{IFT}\{\cos[W_e(\vec{q'})]\mathrm{e}^{+\mathrm{i}W_o(\vec{q'})})\}.
\end{aligned}
\tag{4.22}
$$

The intensity of a wave can be expressed as:

$$
\mathrm{Intensity}(\vec{r'}) = \psi_{\mathrm{det}}(\vec{r'})\overline{\psi_{\mathrm{det}}}(\vec{r'}).
\tag{4.23}
$$

The intensity can be written as CTF, which is normalized to values from -1 to 1.

After a thorough calculation, which can be found in the Appendix, the intensity expressed in CTF can be written in reciprocal coordinates in the form:

$$
\begin{aligned}
\mathrm{CTF}_{\mathrm{ideal}}(\vec{q'}) &= \delta(\vec{q'}) + 2\{E(\vec{q'})\cos[W_e(\vec{q'}) + W_o(\vec{q'})] \\
&\quad + \Phi(\vec{q'})\sin[W_e(\vec{q'}) + W_o(\vec{q'})]\} + \mathcal{O}(\vec{q'}),
\end{aligned}
\tag{4.24}
$$

where $\mathcal{O}(\vec{q'})$ represents the non-linear terms c_2, c_3, c_4 and c_5 which are described in Eq. 8.14 in the Appendix. These terms cannot be analytically or numerically evaluated in general if the only knowledge of the functions $E(\vec{q'})$ and $\Phi(\vec{q'})$ is that they are real functions. The determination of these terms by simulation or other techniques is not part of this bachelor thesis.

In the following part, only thin amorphous carbon sample (thickness ≤ 5 nm) will be discussed.

A simplified formula used in most scientific texts is called linear approximation:

$$\text{CTF}_{\text{ideal,linear}}(\vec{q'}) = |\psi_{\text{det}}(\vec{q'})|^2 = \delta(\vec{q'}) + 2\Phi(\vec{q'}) \sin[W_e(\vec{q'})], \tag{4.25}$$

where non-linear terms and amplitude object function $E(\vec{q'})$ are neglected.

This intensity would be observed if there were a perfect electron source, a perfectly stable current through the lens, and a detector without imperfections.

4.2. Envelope Functions

$\text{CTF}_{\text{ideal}}(\vec{q'})$ is an ideal case. Due to microscope imperfections, Eq. 4.25 must be multiplied by a damping envelope function $\mathbf{E}(q')$, which describes these particular imperfections. The envelope function consists of multiple terms which have a bigger impact on higher spatial frequencies.

Introduction of system instability, finite source brightness, and aberrations impact to illumination is done via envelope function damping $\text{CTF}_{\text{ideal}}(\vec{q'})$ as follows: E_{s} is spatial damping envelope, E_{t} is temporal damping envelope, E_{d} is sample drift envelope, and E_{u} is specimen vibration envelope.

Optical CTF function can be written as:

$$\text{CTF}_{\text{optical}}(\vec{q'}) = E_{\text{s}}(q')E_{\text{t}}(q')E_{\text{d}}(q')E_{\text{u}}(q') \cdot \text{CTF}_{\text{ideal}}(\vec{q'}). \tag{4.26}$$

E_{d} and E_{u} are not considered in this study due to the limited impact visible-drift correction algorithm suppress to non-significant value.

Studied CTF function is in the form of:

$$\text{CTF}_{\text{optical,simplified}}(\vec{q'}) = E_{\text{s}}(q')E_{\text{t}}(q') \cdot \text{CTF}_{\text{ideal}}(\vec{q'}). \tag{4.27}$$

The envelope function dampens the intensity of the wave, meaning that spatial frequencies from a certain point onward are no longer observable.

The temporal envelope function can be written as [19]:

$$E_{\text{t}}(q') = \exp\left[-\frac{1}{2}\pi^2\lambda^2\Delta C_{\text{C}}^2(q')^4\right], \tag{4.28}$$

where ΔC_{C} represents chromatic focus spread which can be written as:

$$\Delta C_{\text{C}} = C_{\text{C}} \cdot H = C_{\text{C}}\sqrt{\left(\frac{\Delta U}{U}\right)^2 + 4\left(\frac{\Delta I}{I}\right)^2 + \left(\frac{\Delta E_{\text{rms}}}{E_0}\right)^2}, \tag{4.29}$$

where C_{C} represents chromatic aberration, $\Delta U/U$ represents instability of the high voltage, $\Delta I/I$ represents the instability of the lens current, $\Delta E_{\text{rms}}/E_0$ represents root-mean-square energy spread of the electron beam which can be calculated as $\Delta E/2\sqrt{2\ln 2}$, where ΔE is the energy spread and where H represents the terms under the square root.

The spatial envelope function is caused by the finite size of the electron source [19]:

$$E_s(q') = \exp\left[-\frac{\pi^2\theta_s^2}{\lambda^2}(\nabla\chi(\vec{q'}))^2\right], \tag{4.30}$$

where θ_s represents the beam divergence semi-angle caused by an aperture and ∇ represents the gradient of function $\chi(\vec{q'})$.

Other types of envelope function are caused by external environmental influences or microscope imperfections such as vibration or sample drift [21]. Sample drift envelope function can be described as [21]:

$$E_d(q') = \text{sinc}(\pi q' d) \approx \exp\left[-\frac{1}{6}(\pi q' d)^2\right], \tag{4.31}$$

where $d = vt_{\exp}$ is total drift, v is linear sample drift speed, $t_{\exp}$ is exposure time.

Specimen vibration envelope function can be written as [21]:

$$E_u(q') = J_0(2\pi q' u) \approx \exp\left[-(\pi q' u)^2\right], \tag{4.32}$$

where J_0 represents a Bessel function of zero order and u represents the amplitude of the vibrations.

In the practice, the biggest influence is related to the spatial and temporal envelope function. In the following text, parallel illumination is used so θ_s is equal to zero and $E_s(q')$ is equal to 1 consequently. This implies that only the temporal envelope function will have an influence on the observed image and $\text{CTF}_{\text{optical}}(\vec{q'})$ is given as:

$$
\begin{aligned}
\text{CTF}_{\text{optical}}(\vec{q'}) = E_t(q')\{\delta(\vec{q'}) + 2\{E(\vec{q'})\cos[W_e(\vec{q'}) + W_o(\vec{q'})] \\
+ \Phi(\vec{q'})\sin[W_e(\vec{q'}) + W_o(\vec{q'})]\} + \mathcal{O}(\vec{q'})\}.
\end{aligned}
\tag{4.33}
$$

4.3. Camera Imaging Impact

$\text{CTF}_{\text{optical}}(\vec{q'})$ is imaged on the detector. Read-out data are modified by camera properties such as detection quantum efficiency, read-out noise, shot-noise dark current, and electron flux.

The best possible resolution which can be obtained is limited by the pixel size and magnification. For example, if the pixel size is $a = 14\,\mu\text{m}$ and magnification is $M = 140,000\text{x}$, the highest theoretical resolution is $a/M = 1$ Å [19].

This resolution is usually not reachable due to the fact that the electron may transfer to multiple photons, which may cause the information to spread from one pixel to multiple pixels. In real coordinate $\vec{r'}$, this phenomenon is called the point spread function on detector (PSF) [19]. To describe this blurring in reciprocal space, we introduce the modulation transfer function (MTF), where the domain in which the function has meaning can be described by the Nyquist frequency $f_N = 1/2a$ [19], where a represents the pixel size in real space.

Another limiting resolution parameter is the detection quantum efficiency which is defined as [8]:

$$\text{DQE} = \frac{\left(\frac{S}{N}\right)_{\text{out}}^2}{\left(\frac{S}{N}\right)_{\text{in}}^2}, \tag{4.34}$$

where the fraction S/N represents the signal-to-noise ratio. The equation for the DQE with respect to spatial frequency can be written as [22]:

$$\text{DQE}(\vec{q'}) = \text{DQE}(0)\frac{\text{MTF}^2(\vec{q'})}{\mathcal{N}(\vec{q'})}, \tag{4.35}$$

where $\mathcal{N}(\vec{q'})$ represents normalised noise power spectrum.

Ideal detector has the DQE(0) = 1 and $\text{MTF}(\vec{q'}) = \text{sinc}(\pi\vec{q'}/2)$. In an ideal detector, the DQE can be written as [22]:

$$\text{DQE}(\vec{q'}) = \text{sinc}^2(\pi\vec{q'}/2). \tag{4.36}$$

The resulting formula for what can be observed as an output on a PC monitor can be described by the following equation [23]:

$$\begin{aligned}
\text{Intensity}_{\text{ob}}(\vec{r'}) = \text{I}_{\text{rn}} &+ \text{I}_{\text{dc}} + \text{CF} \\
&\cdot \text{IFT}\left[\text{FT}\left[P_{\text{oiss}}\left(\Phi_{\text{e}} \cdot \text{IFT}^{-1}\left[\text{CTF}_{\text{optical}}(\vec{q'})\sqrt{\text{DQE}(\vec{q'})}\right]\right)\right] \cdot \text{NTF}(\vec{q'})\right],
\end{aligned} \tag{4.37}$$

where I_{rn} represents the readout noise, I_{dc} is the dark current, CF stands for conversion factor, expressed in ADU(analog-to-digital)/e$^-$, $P_{\text{oiss}}(A)$ represents Poisson noise yield, Φ_{e} is the incident electron flux, measured in [e$^-$ / pixel], $\text{DQE}(\vec{q'})$ stands for detection quantum efficiency and $\text{NFT}(\vec{q'})$ represents the noise transfer function, which can be translated as a non-elastic contribution to the sample imaging.

The simplified graphical interpretation of the normalized observed intensity in reciprocal coordinate can be seen in Fig. 4.2.
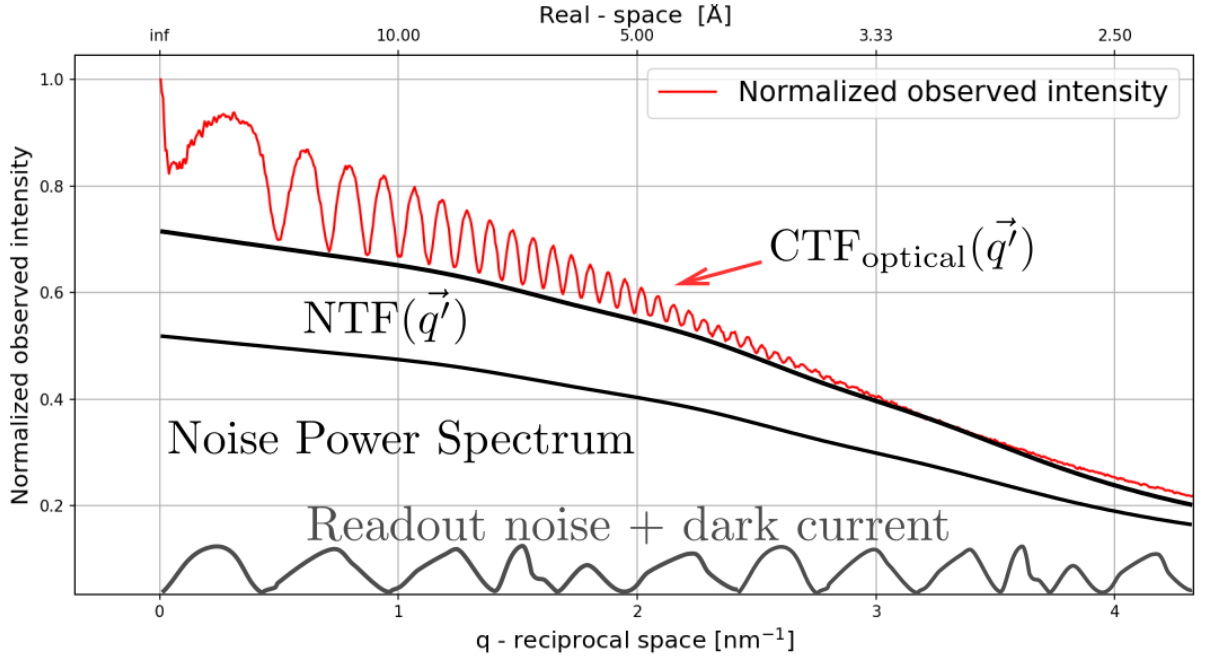

Figure 4.2: Scheme of the normalized observed intensity.

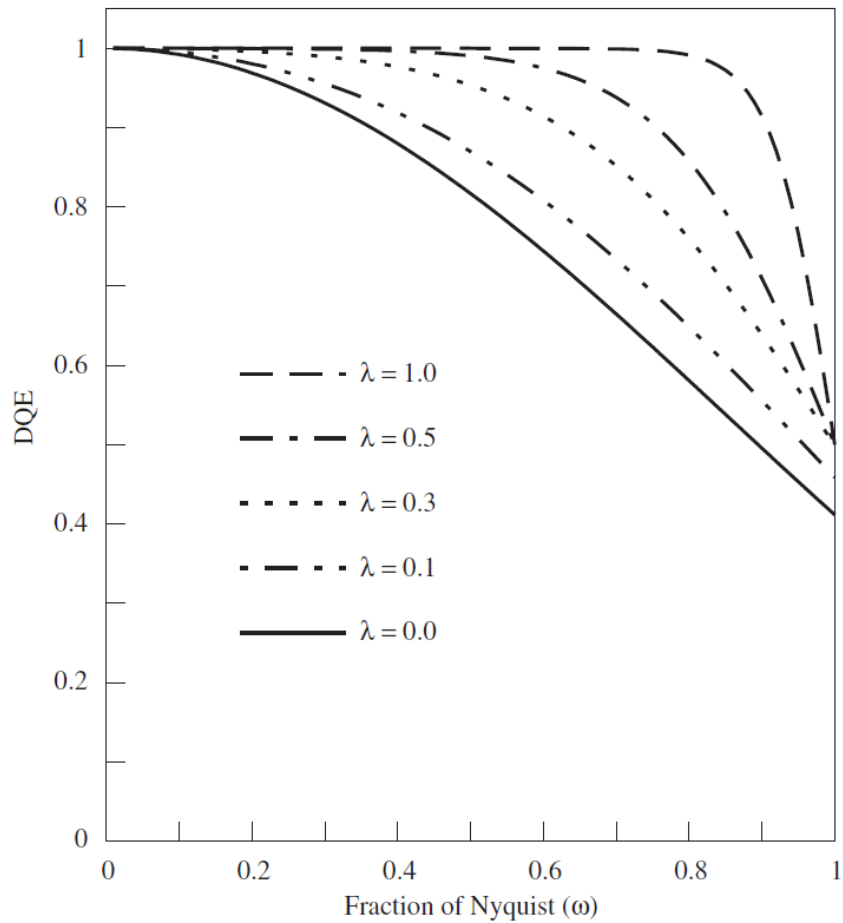Figure 4.3: Shapes for different DQE depending on deterministic blur λ, adapted from [22].

5. Non-linear Imaging

5.1. Reasons for Lower Accelerating Voltage

In recent history, there have been studies about lowering the accelerating voltage from 300 kV to 100 kV or even lower to 60 or 80 kV [24]. Possible benefits could be increasing the lifespan [25] of an observed sample in terms of useable information, gaining contrast, and, more importantly, making it more affordable for smaller research teams.

The dependence of the sample damage on the accelerating voltage affects the amount of information we can extract from the observed sample. It has been shown [26] that reducing the accelerating voltage from 300 kV to 100 kV can increase the quantity of usable information from certain samples by 25%, which is quite substantial.

Despite all the positives, certain problems arise with decreasing accelerating voltage. The pixel size of an imaging device as a detector or a camera designed for an accelerating voltage of 300 kV has to be different for a lower accelerating voltage due to the process of electron scattering at the detector sensitive area and the subsequent information readout [24]. The solution to the problem could be to increase the pixel size by combining a grid of pixels. Unfortunately, this will lead to a smaller field of view and other problems. The alternative approach is redesigning the detector to keep the same field of view. Unfortunately, new types of detectors called hybrid pixelated detectors are not at these days at the requiered number of pixels (512 x 512) [27].

Another problem is related to the longer wavelength of the electrons and the more visible influence of chromatic aberration due to the term H in Eq. 4.29. These effects deteriorate the optical properties of the image.

5.2. Imaging at 100 kV - Non-linear Terms

When it comes to an imaging theory that was derived in the chapter 4, in most cases, only the linear terms are taken into account. But during observation and measurements in the electron microscope Tundra Cryo-TEM developed by Thermo Scientific™ [28], the images have shown a better information limit that cannot be explained by the linear approximation. This may lead to the idea that the influence of the non-linear terms is not negligible and that these terms may lead to an explanation of the observed resolution.

To confirm theoretical calculation, experimental data were acquired at 100 kV at Tundra, at 200 kV at Glacios and at 300 kV at Krios developed by Thermo Scientific™.

Another approach to non-linear imaging has been shown and derived in [29]. This derivation takes into account the use of the transmission cross-coefficient. This is not studied in this work.

6. Experimental Part

6.1. Linear Imaging at Different Accelerating Voltages

Nowadays, 100 kV, 200 kV, and 300 kV TEM are commonly used for SPA. Their CTF are shown in Fig. 6.1a, Fig. 6.1b and Fig. 6.1c. The black curve represents the damping envelope function E_t, while the red curve represents the CTF function. It can be noticed that as the accelerating voltage increases, the positions of the maxima and minima change while the possible observable resolution increases. The information limit $q_{info-limit}$, or the best resolution that can be obtained from the microscope, is defined as [19]:

$$q_{info-limit} \rightarrow E_t = \frac{1}{e^2},$$
(6.1)

where e stands for Euler´s constant.

The conditions of simulation for all of the types of microscopes are described in Tab. 6.1 below, depicting the real systems values. The applied defocus is the same as that used when acquiring the info-limits and is calculated as [8]:

$$C_{1,0;Scherzer} = -\left(\frac{4}{3}C_{3,0}\lambda\right)^{1/2},$$
(6.2)

where $C_{3,0}$ is spherical aberration constant and λ is wavelength of electrons. For info-limit acquisition, 3x Scherzer´s defocus gives the best contrast for high frequencies.

Table 6.1: Parameters of the experiment.

Parameters	Tundra	Glacios	Krios
Accelerating voltage [kV]	100	200	300
Chromatical aberration C_C [mm]	1.7	2.7	2.7
Spherical aberration $C_{3,0}$[mm]	1.6	2.7	2.7
Objective lens [Type]	SP-Twin	C-Twin	C-Twin
Constant H [10^{-6}]	3.15	2.64	1.43
Defocus (3-times Scherzer´s defocus) [nm]	-266	-285	-252

Theoretical values for info-limit calculated by Eq. 4.28 and Eq. 6.1 is shown in Tab. 6.2.

Table 6.2: Theoretical info-limits of systems.

| Microscopes	Tundra	Glacios	Krios
Accelerating voltage [kV]	100	200	300
Theoretical info-limit [Å]	1.9	1.7	1.2

Although Tundra system has the lowest spherical and chromatical aberrations, its info-limit is the lowest one because of its acceleration voltage.

Info-limit images of amorphous carbon with gold particles taken in high resolution from Tundra, Glacios, and Krios are shown in Fig. 6.2a, Fig. 6.2c, and Fig. 6.2e. Fourier transform of these images are shown in Fig. 6.2b, Fig. 6.2d, and Fig. 6.2f, where the green circle represents observed info-limit and the red circle represents theoretical info-limit.
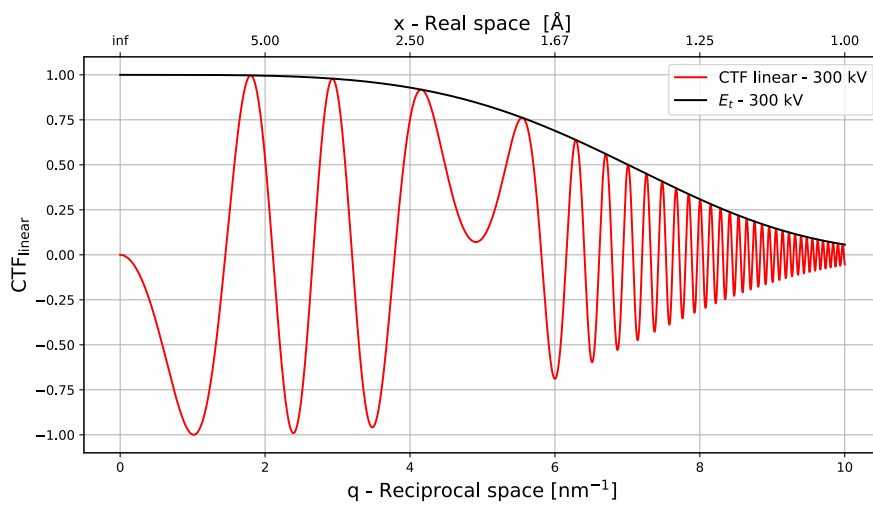
These info-limit images are taken with a small image shift enabling visualization of the real 2D CTF (suppressing the influence of the camera power spectrum $\mathcal{N}(\vec{q})$).
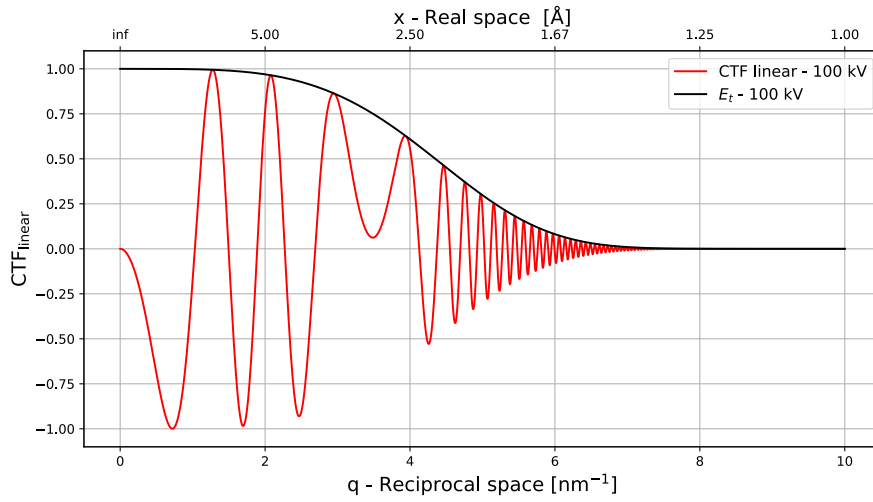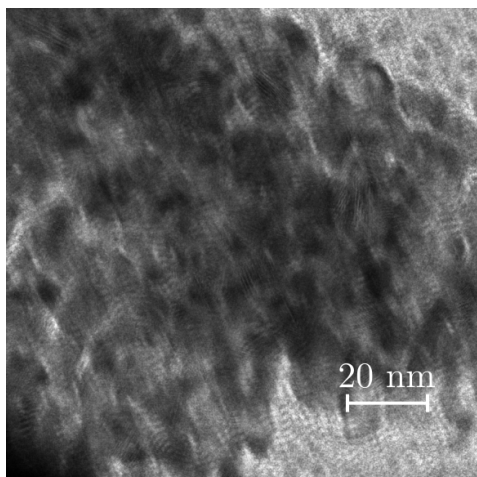
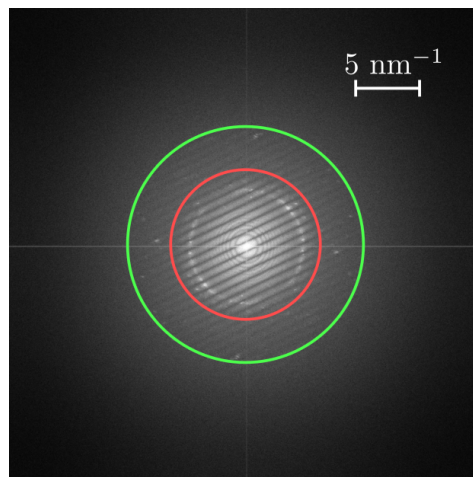(a) Tundra: CTF 100 kV linear.
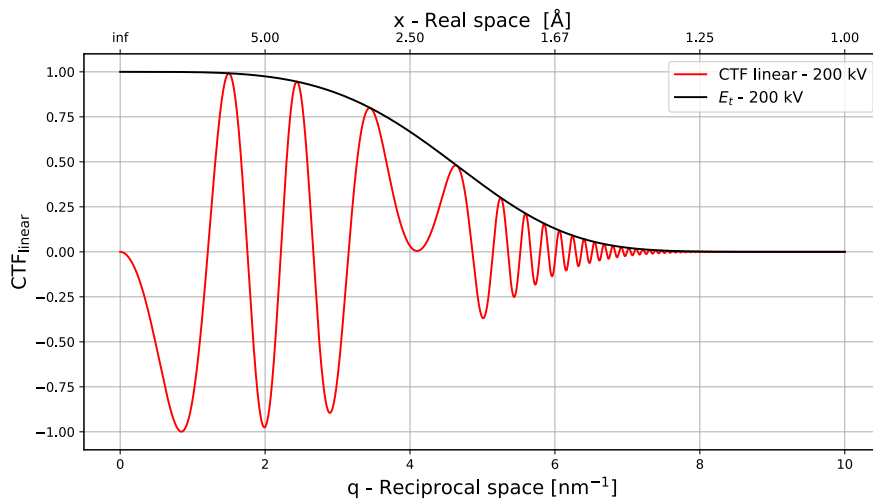
(b) Glacios: CTF 200 kV linear.
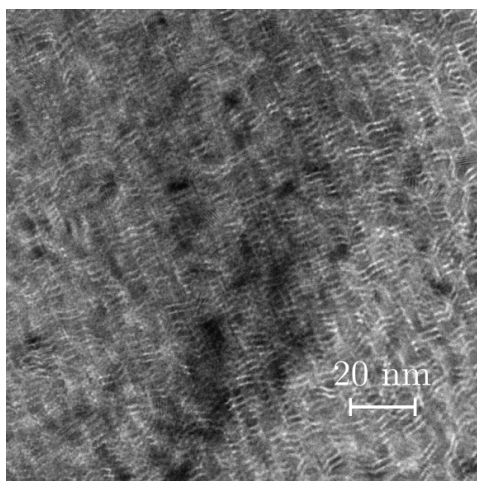

(c) Krios: CTF 300 kV linear.

Figure 6.1: Linear CTFs.

(a) Tundra: Info-limit image at 100 kV at magnification M = 470,000x.

(b) Fourier transform of a sample imaged at 100 kV. Green circle corresponds to 1.2 Å, and red circle to 1.9 Å.

(c) Glacios: Info-limit image at 200 kV at magnification M = 400,000x.

(d) Fourier transform of a sample imaged at 200 kV. Green circle corresponds to 1.4 Å, and red circle to 1.7 Å.

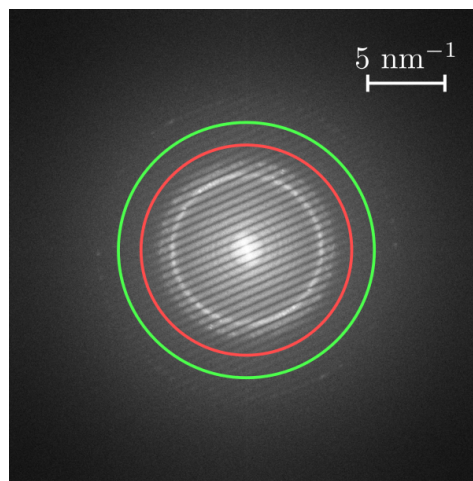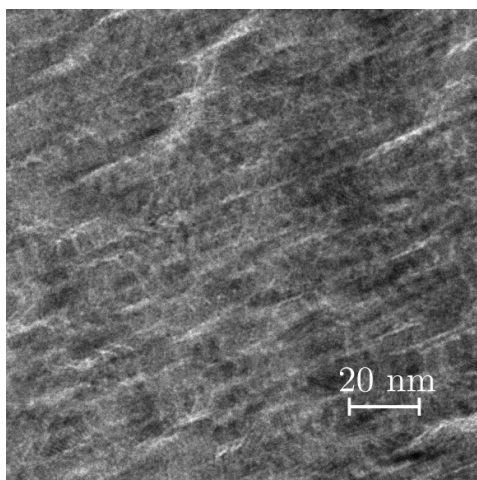
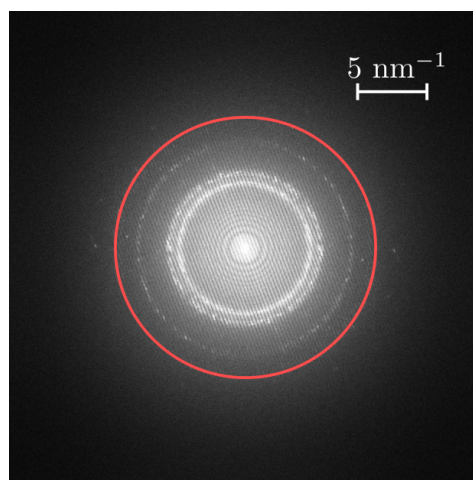(e) Krios: Info-limit image at 300 kV at magnification M = 250,000x.

(f) Fourier transform of a sample imaged at 300 kV. Red circle corresponds to 1.2 Å.

Figure 6.2: Info-limits of amorphous carbon with gold particles for 100, 200 and 300 kV.

6.2. Non-linear Imaging at Different Accelerating Voltages

The linear theory describes imaging performance at 300 keV in good fit but at 200 keV, and 100 keV it starts to deviate from the observed images' resolution. This is well seen in Fig. 6.2b, Fig. 6.2d and Fig. 6.2f.

Real limits of the system derived from Fig. 6.2b, Fig. 6.2d, and Fig. 6.2f are given in Tab. 6.3 and are in contrast with its theoretical values coming from linear imaging.

Table 6.3: Observed info-limits of systems.

Microscopes	Tundra	Glacios	Krios
Accelerating voltage [kV]	100	200	300
Theoretical info-limit [Å]	1.9	1.7	1.2
Observed info-limit [Å]	1.2	1.4	1.2

These deviations can be explained by weak phase sample approximation or by application of only linear terms in imaging theory in Eq. 4.25. Only the influence of non-linear terms is studied in this work.

Investigating the effect of non-linear terms, it is preferable to choose a sample that has a much simpler structure than the aforementioned apoferritin sample located in the buffer. This approach removes crystalline form factors and enables us to focus purely on the imaging part of the equation.

This fact can be observed by comparing the 1D graph in Fig. 6.7a and Fig. 6.7b, where the difference in the observed intensity of the photos is clearly visible.

In this section, the approximation $\Phi(\vec{q}) = \text{konst}$ and $E(\vec{q}) = 0$ [30] is used for the ultra-thin film of amorphous carbon with a thickness of 3 nm.

In order to calculate the value of $\Phi(\vec{q})$ for our sample for different accelerating voltages, the following formula is used [31]:

$$\Phi(\vec{q}) = \sigma(\lambda)v_z(\vec{q}), \tag{6.3}$$

where $v_z(\vec{q})$ represents the atomic potential and $\sigma(\lambda)$ is the interaction parameter which can be calculated as [31]:

$$\sigma(\lambda) = \frac{2\pi me\lambda}{h^2}, \tag{6.4}$$

where m represents the relativistic mass for the electron, e is the electron charge, λ is the wavelength of the electron and h is the Planck's constant.

The approximation that the atomic potential $v_z(\vec{q})$ is equal to a constant for a certain thickness will be used. This constant is determined from the article [30] and is equal to $4.11 \cdot 10^{-8}$ V for 3 nm thin sample.

The value for $\Phi(\vec{q})$ is known from the article for accelerating voltage 200 kV. The values of $\Phi(\vec{q})$ for other accelerating voltages can then be determined using Eq. 6.3 and Eq. 6.4.

Since the function $\Phi(\vec{q})$ grows linearly with thickness and the $\sigma(\lambda)$ is constant for a given voltage, the atomic potential $v_z(\vec{q})$ can also be assumed to grow linearly with thickness.

The dependence of atomic potential on thickness and phase shift at different accelerating voltages on thickness is shown in Fig. 6.3a and Fig. 6.3b.
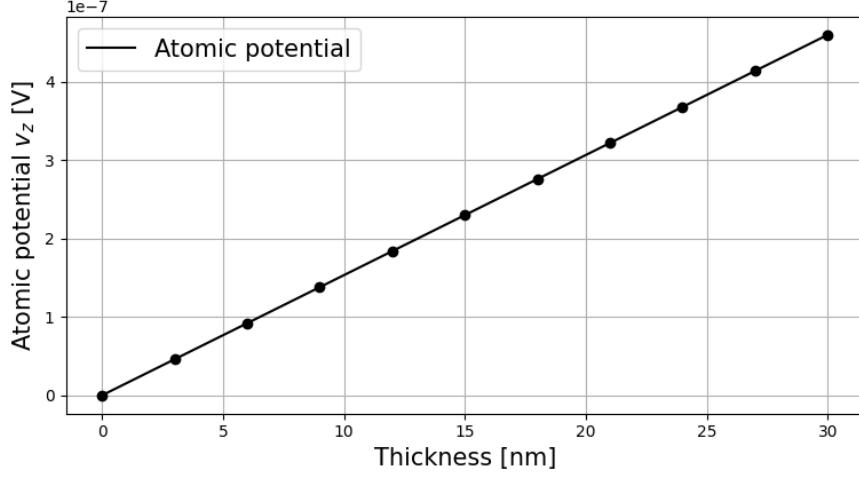
(a) Atomic potential of amorphous carbon.

(b) Phase shift of amorphous carbon for different accelerating voltages.

Figure 6.3: Properites of amorphous carbon, derived from [30].

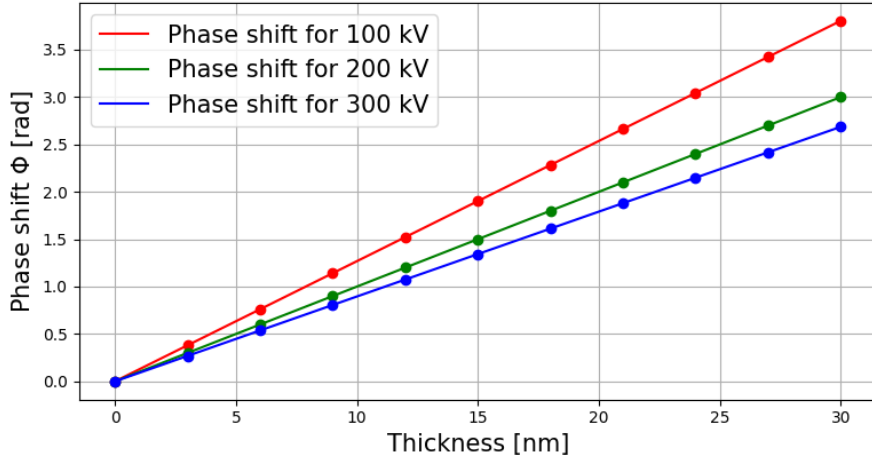This resulted in the final form of the optical intensity, including the remaining non-linear terms, as follows:

$$
\begin{aligned}
\text{CTF}_{\text{optical}}(\vec{q'}) = E_{\text{t}}(q')\{\delta(\vec{q'}) + 2\Phi(\vec{q'})\sin[W_e(\vec{q'})] + \Phi^2(\vec{q'})\sin[W_e(\vec{q'})] \otimes \sin[W_e(\vec{q'})] \\
+ \Phi^2(\vec{q'})\cos[W_e(\vec{q'})] \otimes \cos[W_e(\vec{q'})]\}.
\end{aligned}
\tag{6.5}
$$

The effect of these non-linear terms is shown in Fig. 6.4a, Fig. 6.4b and Fig. 6.4c. In a comparison of Fig. 6.1a and Fig. 6.4a, the non-linear terms have a major influence in the region between 0 and 2 nm^{-1} and in the region between 4.5 and 7 nm^{-1}.

Because of the influence of the temporal envelope function and the small $\Phi(\vec{q'})$ function for the studied sample, which is furthermore squared, unfortunately, these non-linear terms are damped to such an extent that they fail to fully explain the corresponding effect on the observed resolution.
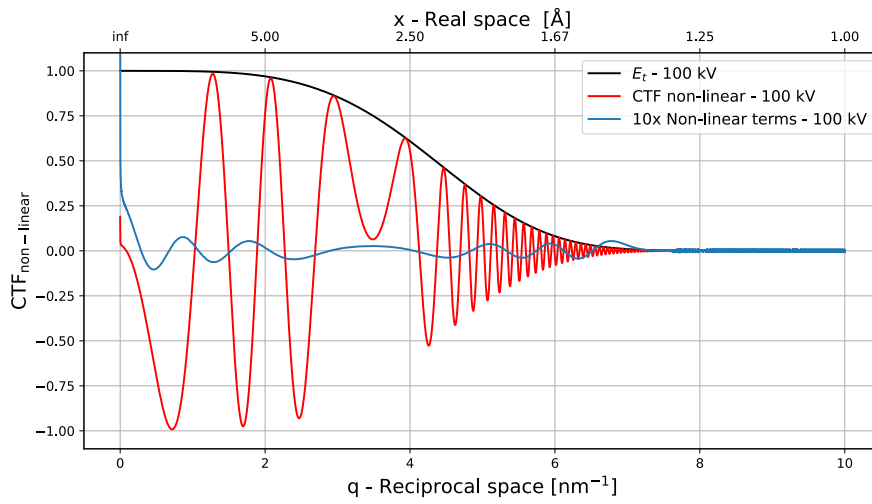
(a) Tundra: CTF 100 kV non-linear.
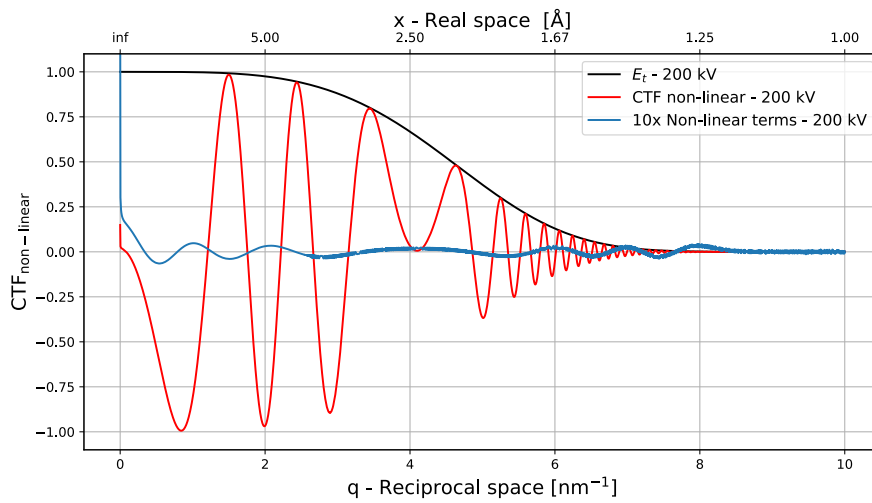
(b) Glacios: CTF 200 kV non-linear.
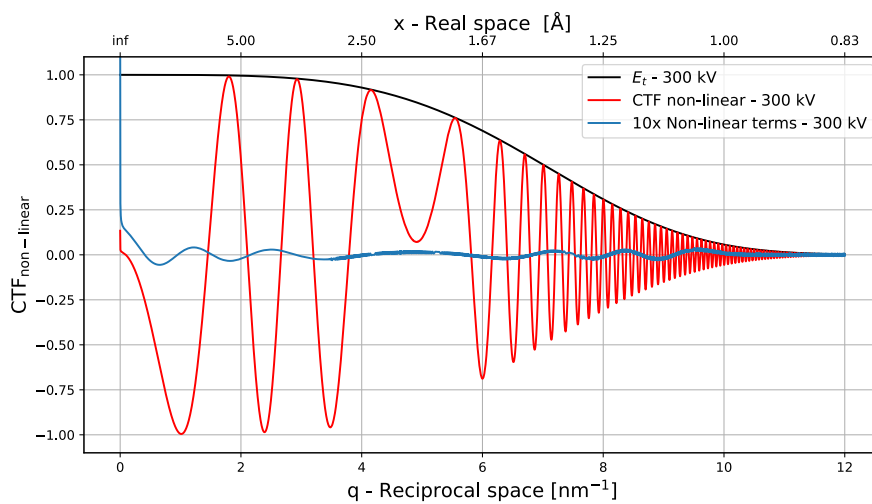
(c) Krios: CTF 300 kV non-linear.

Figure 6.4: Non-linear CTFs.

To better understand the effect of the non-linear terms on the different accelerating voltages, plots describing the relative difference between CTF non-linear and CTF linear are shown.

During observations at an accelerating voltage of 300 kV, higher resolution than theoretically possible has not been reported, which may indicate that the influence of non-linear terms is negligible in this case.

This might be a problem nowadays, mainly for a reason already mentioned above, which is that scientists are trying to change to lower and lower accelerating voltages [24].

The non-linear CTF imaging calculation was performed under the aforementioned assumption of a 3 nm thin amorphous carbon film. Its CTF for 100, 200, and 300 kV is shown in Fig. 6.4a, Fig. 6.4b, and Fig. 6.4c. The non-linear terms are magnified 10x to make the shape of the function more visible.

The non-linear optical terms have the strongest influence at 100 kV, and it is almost negligible for 300 kV. Still, its absolute value cannot fully explain the observed info-limit below the theoretical info-limit seen on the image on a real system.

Unfortunately, the exact determination of the terms cannot be done analytically in general. A possible solution may be to use a linear approximation to determine the defocus of $C_{1,0}$ at lower spatial frequencies, then the functions $E(\vec{q})$ and $\Phi(\vec{q})$, and then these determined values can be plugged into the terms c_2 to c_5 mentioned in Eq. 8.14. Then the convolution could be calculated, and thus, the non-linear terms determined.

6.3. Data from the Systems

SPA data are acquired under different conditions than info-limit. It is done in this way to enhance contrast at lower spatial frequencies. This enables correct orientation categorizing and consequently the better 3D resolution of the imaged particles. Defocus in few μm was used to take testing pictures simulating SPA acquisition setup (so called Thon rings) in Fig. 6.6b. A specific optical setup for SPA acquisition is parallel illumination and defocus −1 μm for SP-Twin and −2 μm for C-Twin.

The sample selected for this study was apoferritin and an ultra-thin film of amorphous carbon. Apoferritin is an iron-free variant of ferritin and has enormous potential in medicine as, for example, a nano transporter. One of the biggest advantages of ferritins is that they are present in the bodies of organisms, unlike other possible candidates such as fullerene and other nanomaterials [32]. Nowadays, it is used as a golden standard to verify bio EM resolution. Unfortunately apoferritin samples quality varies significantly and cannot be used to evaluate the system's optical performance with high confidence.

Amorphous carbon was chosen because of its standardized high quality (homogeneity and thickness) and its high electron dose resistivity, enabling high-resolution imaging. The difference between the two structures of apoferritin and amorphous carbon becomes apparent in the Fig. 6.5b, Fig. 6.6b, Fig. 6.7a, and Fig. 6.7b.

In Fig. 6.5a, we can see particles of apoferritin located in a buffer imaged at 180,000x magnification, and Fig. 6.5b shows the Fourier transform of the corresponding image.

The experimental conditions for info-limit images of the microscopes are described in Tab. 6.1.

To find out the the impact of the non-linear terms on the image resolution, amorphous carbon and apoferritin are investigated. The difference in intensity observation, which is
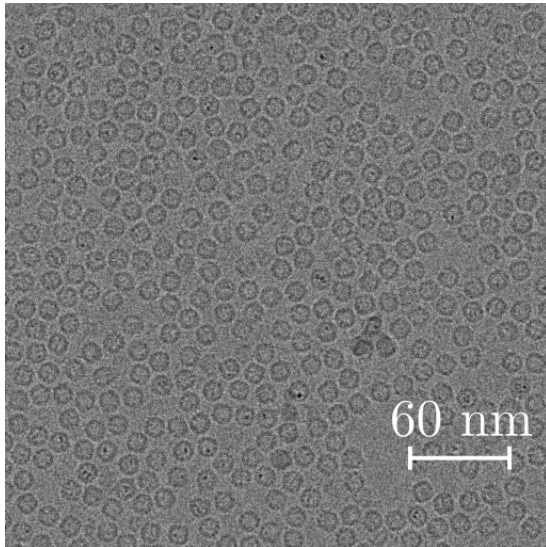
(a) Tundra: Depiction of many apoferritin molecules imaged at 100 kV and 180,000x magnification.
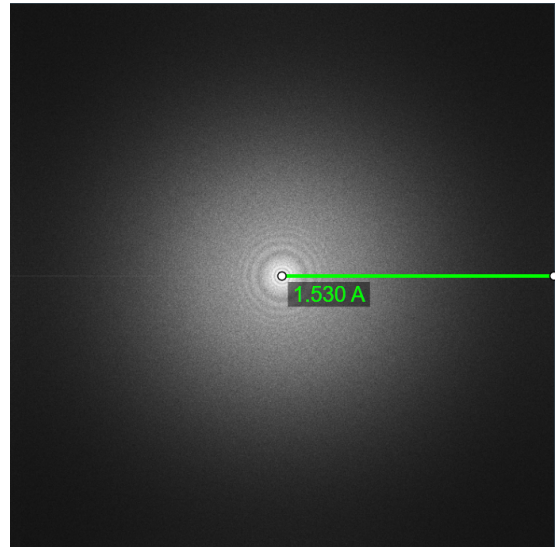
(b) Fourier transform of apoferritin molecules imaged at 100 kV and 180,000x magnification.

Figure 6.5: Tundra: Image and Fourier transform of apoferritin.

normalized from 0 to 1 for easier direct interpretation, between the amorphous carbon and apoferritin samples is clearly visible in Fig. 6.7a and Fig. 6.7b showing the 1D profile of the Fourier transform described by the Eq. 4.37, only converted to reciprocal coordinates, from each sample as a function of spatial frequencies. The magnitude of the intensity at zero is due to the delta function, which appears in the calculation in Eq. 4.24.

Fig. 6.6a shows a photo of amorphous carbon taken at a magnification of 140,000x, and Fig. 6.6b represents its Fourier transform. The distance from the center to the edge of the FFT corresponds to the Nyquist frequency, which was described in chapter 4.

(a) Tundra: Amorphous carbon displayed at 100 kV and 140,000x magnification.
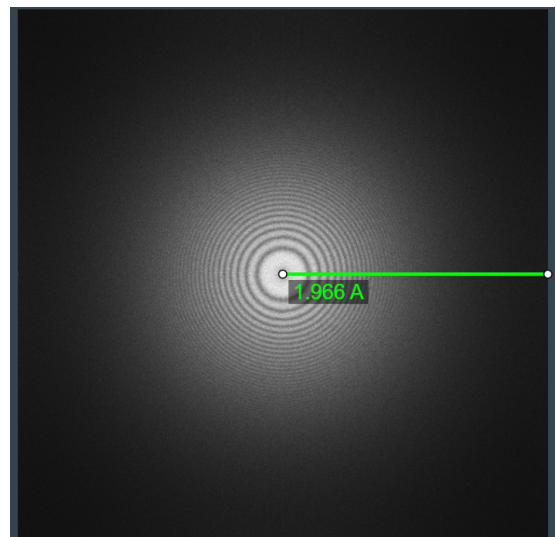
(b) Fourier transform of amorphous carbon at 100 kV and 140,000x magnification.

Figure 6.6: Tundra: Image and Fourier transform of amorphous carbon.
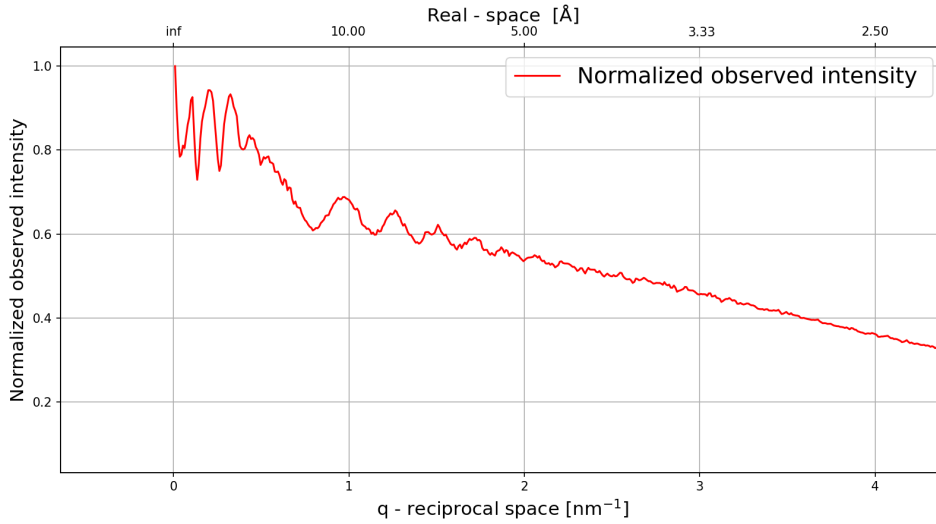
(a) Tundra: 1D graph representing the normalized observed intensity of apoferritin molecules displayed at 100 kV and 180,000x magnification.
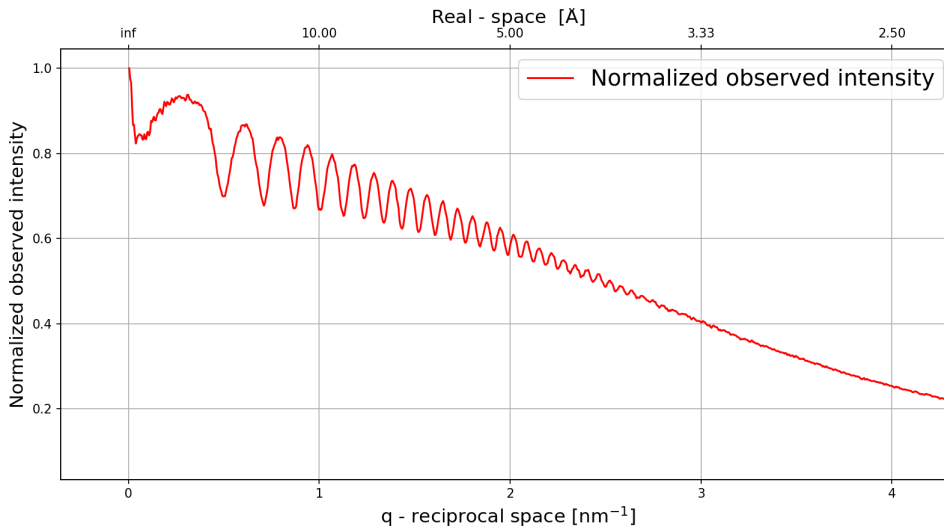
(b) Tundra: 1D graph representing the normalized observed intensity of amorphous carbon displayed at 100 kV and 140,000x magnification.
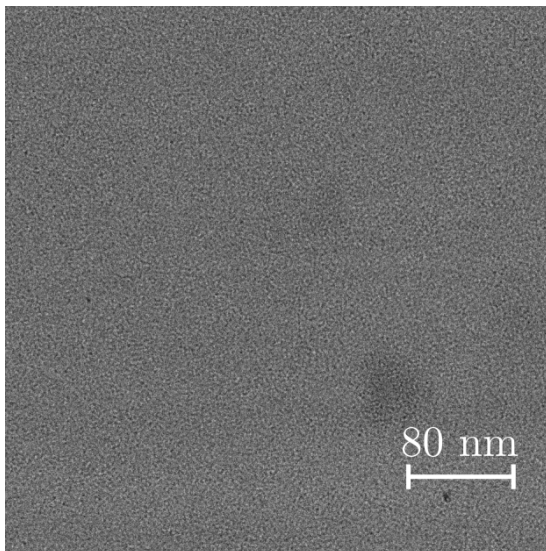
Figure 6.7: Tundra: 1D graphs of normalized observed intensity.

After taking photos of apoferritin and amorphous carbon, a 1D plot of the observed intensity can be made. This is done by summing the intensity values from points equidistant from the center of the 2D FFT plot, which is carried out by switching from Cartesian coordinates to polar coordinates. The programming language Python was used for rendering all of the 1D graphs.

The different Nyquist frequency of the individual photos is due to the fact that the photos of apoferritin and carbon were taken at different magnifications.

Fig. 6.7a and Fig. 6.7b show 1D profiles of the normalized observed intensity obtained from the Fourier transform. It is clearly seen that the amorphous carbon sample enables more accurate fitting of CTF to measured data in comparison to the apoferritin sample.

However, it is crucial to know all parameters of Eq. 4.37 to make a solid CTF derivation - mainly in region of high resolution (in Fig. 6.7b above 2 nm^{-1}).

Only magnification M = 140,000x does not allow the revealing of the smallest detectable details due to camera DQE. Therefore, a higher magnification must be chosen where the possible info-limit is encountered. Fig. 6.2b again shows a sample of amorphous carbon, where it is already visible that using the classical linear approximation does not explain the observed intensity, which represents the resolution of $\approx$ 1.2 Å. Thus, the influence of non-linear terms are investigated. As it is visible in Fig. 6.4a, only optical non-linear terms cannot explain this resolution of 1.2Å.

Another possible explanation of observed intensity may be that we cannot treat the functions $E(\vec{q})$ and $\Phi(\vec{q})$ purely in linear approximation of Eq. 4.4, as was the case in this bachelor thesis.

7. Conclusion

In this bachelor thesis, the problems of TEM as a system, methods of preparation of biological samples, and the theoretical description and derivation of imaging in TEM were presented. The CTF of the observed image was calculated, including the possible influence of sample absorption and non-linear terms, which were determined to be impossible to calculate analytically without detailed knowledge of the individual functions $E(\vec{q'})$ and $\Phi(\vec{q'})$. Subsequent calculations had to be done numerically after further approximations.

Furthermore, CTF functions, where only linear terms were included, were compared for 100, 200, and 300 kV systems. The influence of non-linear terms was then shown in the representation of amorphous carbon observed at an accelerating voltage of 100, 200, and 300 kV. However, these terms alone failed to fully determine the observed resolution.

The observed resolution cannot be explained only by non-linear optical terms of CTF. Further investigation can be focused on non-linear sample electron interaction approximation.

SPA imaging is not impacted as significantly as info-limit mainly because of smaller used magnification concluding in lower image spatial resolution.

A possible follow-up topic, e.g., for a diploma thesis, might be the procedure for the general determination of just the functions $E(\vec{q})$ and $\Phi(\vec{q})$ from measured data without any knowledge of the observed material.

Bibliography

[1] FALCONER, Isobel. JJ Thomson and the discovery of the electron. *Physics Education*, 1997, 32.4: 226. ISSN 0031-9120. Available from DOI: 10.1088/0031-9120/32/4/015.

[2] BONNAR, James. A Short Note on the de Broglie Wavelengths of Composite Objects. ISSN unknown.

[3] ROSE, Harald H. Optics of high-performance electron microscopes. *Science and Technology of Advanced Materials*, 2008, 9.1: 014107. ISSN 1468-6996, Available from DOI: 10.1088/0031-8949/9/1/014107.

[4] THOMSON, George Paget. Experiments on the diffraction of cathode rays. *Proceedings of the Royal Society of London. Series A, containing papers of a mathematical and physical character*, 1928, 117.778: 600-609. ISSN 0950-1207. Available from DOI: 10.1098/rspa.1928.0022.

[5] RUSKA, Ernst. The development of the electron microscope and of electron microscopy. *Reviews of modern physics*, 1987, 59.3: 627. ISSN 0034-6861. Available from DOI: 10.1103/RevModPhys.59.627.

[6] CHEN, Zhen, et al. Electron ptychography achieves atomic-resolution limits set by lattice vibrations. *Science*, 2021, 372.6544: 826-831. ISSN 0036-8075. Available from DOI: 10.1126/science.abg2533.

[7] SHÁNĚL, O.: *Tolerances and misalignment aberrations for electron optical elements and systems* [doctoral thesis]. Brno: Brno University of Technology, Faculty of Mechanical Engineering, 2014, 87 p.

[8] WILLIAMS, D. B.; CARTER, C. B.: *Transmission electron microscopy: a textbook for materials science.* 2nd ed. New York: Springer, 2009. ISBN 978-0-387-76500-6.

[9] REIMER, L.; KOHL, H.: *Transmission electron microscopy: physics of image formation.* 5th ed. New York: Springer, 2008. ISBN 978-0-387-40093-8.

[10] SANTUCCI, Alessia, et al. Novel non-evaporable getter materials and their possible use in fusion application for tritium recovery. *Molecules*, 2020, 25.23: 5675. ISSN 1420-3049. Available from DOI: 10.3390/molecules25235675.

[11] WU, Mengyu; LANDER, Gabriel C. Present and emerging methodologies in cryo-EM single-particle analysis. *Biophysical journal*, 2020, 119.7: 1281-1289. ISSN 0006-3495. Available from DOI: 10.1016/j.bpj.2020.08.027.

[12] *PDB Statistics.* Available also from: https://www.rcsb.org/stats/.

[13] SHEN, Peter S. The 2017 Nobel Prize in Chemistry: cryo-EM comes of age. *Analytical and bioanalytical chemistry*, 2018, 410: 2053-2057. ISSN 1618-2642. Available from DOI: 10.1007/s00216-018-0899-8.

BIBLIOGRAPHY

[14] FRANK, Joachim. Generalized single-particle cryo-EM–a historical perspective. *Journal of Electron Microscopy*, 2015, 65.1: 3-8. ISSN 2050-5698. Available from DOI: 10.1093/jmicro/dfv358.

[15] NAKANE, Takanori, et al. Single-particle cryo-EM at atomic resolution. *Nature*, 2020, 587.7832: 152-156. ISSN 0028-0836. Available from DOI: 10.1038/s41586-020-2829-0.

[16] DOBRO, Megan J., et al. Plunge freezing for electron cryomicroscopy. *Methods in enzymology*, 2010, 481: 63-82. ISSN 0076-6879 . Available from DOI: 10.1016/S0076-6879(10)81003-1.

[17] SGRO, Germán G.; COSTA, Tiago RD. Cryo-EM grid preparation of membrane protein samples for single particle analysis. *Frontiers in molecular biosciences*, 2018, 5: 74. ISSN 2296-889X. Available from DOI: 10.3389/fmolb.2018.00074.

[18] CARRONI, Marta; SAIBIL, Helen R. Cryo electron microscopy to determine the structure of macromolecular complexes. *Methods*, 2016, 95: 78-85. ISSN 1046-2023. Available from DOI: 10.1016/j.ymeth.2015.11.023

[19] ERNI, Rolf. Aberration-corrected imaging in transmission electron microscopy: An introduction. *World Scientific Publishing Company*, 2015. ISBN 978-1-78326-528-2.

[20] ORLOFF, Jon, et al.: *Handbook of charged particle optics*. CRC Press; Taylor & Francis, 2009. ISBN 978-1-4200-4554-3.

[21] DE JONG, A. F.; VAN DYCK, D. Ultimate resolution and information in electron microscopy II. The information limit of transmission electron microscopes. *Ultramicroscopy*, 1993, 49.1-4: 66-80. ISSN 0304-3991. Available from DOI: 10.1016/0304-3991(93)90213-H.

[22] MCMULLAN, G., et al. Detective quantum efficiency of electron area detectors in electron microscopy. *Ultramicroscopy*, 2009, 109.9: 1126-1143. ISSN 0304-3991. Available from DOI: 10.1016/j.ultramic.2009.04.002.

[23] VULOVIĆ, Miloš, et al. Image formation modeling in cryo-electron microscopy. *Journal of structural biology*, 2013, 183.1: 19-32. ISSN 1047-8477. Available from DOI: 10.1016/j.jsb.2013.05.008.

[24] NAYDENOVA, K., et al. CryoEM at 100 keV: a demonstration and prospects. *IUCrJ*, 2019, 6.6: 1086-1098. ISSN 2052-2525. Available from DOI: 10.1107/S2052252519012612.

[25] BÖRRNERT, Felix, et al. Engineering the Contrast Transfer through the Cc/Cs Corrected 20-80 kV SALVE Microscope. *Microscopy and Microanalysis*, 2016, 22.S3: 880-881. ISSN 1431-9276. Available from DOI: 10.1017/S1431927616005249.

[26] PEET, Mathew J.; HENDERSON, Richard; RUSSO, Christopher J. The energy dependence of contrast and damage in electron cryomicroscopy of biological molecules. *Ultramicroscopy*, 2019, 203: 125-131. ISSN 0304-3991. Available from DOI: 10.1016/j.ultramic.2019.02.007.

[27] VAN SCHAYCK, J. Paul, et al. Integration of an event-driven timepix3 hybrid pixel detector into a cryo-em workflow. *Microscopy and Microanalysis*, 2023, 29.1: 352-363. ISSN 1431-9276. Available from DOI: 10.1093/micmic/ozac009.

[28] HLAVENKOVÁ, Zuzana, et al. Thermo Scientific™ Tundra Cryo-TEM: 100kV Cryo-TEM dedicated for Single Particle Analysis. *Microscopy and Microanalysis*, 2021, 27.S1: 1330-1332. ISSN 1431-9276. Available from DOI: 10.1017/S1431927621004967.

[29] ISHIZUKA, Kazuo. Contrast transfer of crystal images in TEM. *Ultramicroscopy*, 1980, 5.1-3: 55-65. ISSN 0304-3991. Available from DOI: 10.1016/0304-3991(80)90011-X.

[30] RICOLLEAU, C., et al. Random vs realistic amorphous carbon models for high resolution microscopy and electron diffraction. *Journal of Applied Physics*, 2013, 114.21: 213504. ISSN 0021-8979. Available from DOI: 10.1063/1.4831669.

[31] KIRKLAND, Earl J. *Advanced Computing in Electron Microscopy.* Springer Science & Business Media, 2010. ISBN 978-1-4419-6532-5.

[32] HEGER, Zbynek, et al. Apoferritin applications in nanomedicine. *Nanomedicine*, 2014, 9.14: 2233-2245. ISSN 1743-5889. Available from DOI: 10.2217/nnm.14.119.

8. Appendix

In the appendix, the intensity of the wave will be calculated.
Intensity of a wave can be expressed as:

$$\text{Intensity}(\vec{r}^{\,\prime\prime}) = \psi_{\text{det}}(\vec{r}^{\,\prime\prime})\overline{\psi_{\text{det}}}(\vec{r}^{\,\prime\prime}). \tag{8.1}$$

Some of the useful trigonometry identities which are used in the following derivations:

$$e^{+iW_o(\vec{q'})} + e^{-iW_o(\vec{q'})} = 2\cos[W_o(\vec{q'})],$$
$$e^{+iW_o(\vec{q'})} - e^{-iW_o(\vec{q'})} = 2i\sin[W_o(\vec{q'})],$$
$$2\cos(x)\sin(y) + 2\cos(y)\sin(x) = 2\sin(x+y),$$
$$2\cos(x)\cos(y) - 2\sin(x)\sin(y) = 2\cos(x+y),$$

Other formulas that may be useful in the following calculations are listed below. These are formulas that describe the identities for functions and their fourier transforms, especially in terms of multiplication and convolution operations.

$$f \otimes g + f \otimes h = f \otimes (g+h) \tag{8.2}$$

$$\text{FT}\{g \otimes h\} = \text{FT}\{g\} \cdot FT\{h\} \tag{8.3}$$

$$\text{FT}\{g \cdot h\} = \text{FT}\{g\} \otimes \text{FT}\{h\} \tag{8.4}$$

$$g \otimes h = \text{IFT}\{\text{FT}\{g\} \cdot \text{FT}\{h\}\} \tag{8.5}$$

$$g \cdot h = \text{IFT}\{\text{FT}\{g\} \otimes \text{FT}\{h\}\} \tag{8.6}$$

$$f = \text{IFT}\{\text{FT}(f)\} = \text{FT}\{\text{IFT}(f)\} \tag{8.7}$$

For clearer readability Eq. 8.1 is separated into 5 parts.

$$\text{Intensity}(\vec{r}') = a_1(\vec{r}') + a_2(\vec{r}') + a_3(\vec{r}') + a_4(\vec{r}') + a_5(\vec{r}') \tag{8.8}$$

After initial multiplication of the individual terms, the product is given as follows:

$$
\begin{aligned}
a_1 =\ &1 \\
&+ \epsilon(\vec{r}') \otimes \text{IFT}\{\cos[W_e(\vec{q}')]\mathrm{e}^{+iW_o(\vec{q}')}\} \\
&+ \varphi(\vec{r}') \otimes \text{IFT}\{\sin[W_e(\vec{q}')]\mathrm{e}^{+iW_o(\vec{q}')}\} \\
&+ i\epsilon(\vec{r}') \otimes \text{IFT}\{\sin[W_e(\vec{q}')]\mathrm{e}^{+iW_o(\vec{q}')}\} \\
&- i\varphi(\vec{r}') \otimes \text{IFT}\{\cos[W_e(\vec{q}')]\mathrm{e}^{+iW_o(\vec{q}')}\} \\
a_2 =\ &+\epsilon(\vec{r}') \otimes \text{IFT}\{\cos[W_e(\vec{q}')]\mathrm{e}^{-iW_o(\vec{q}')}\} \\
&+ \epsilon(\vec{r}') \otimes \text{IFT}\{\cos[W_e(\vec{q}')]\mathrm{e}^{-iW_o(\vec{q}')}\} \cdot \epsilon(\vec{r}') \otimes \text{IFT}\{\cos[W_e(\vec{q}')]\mathrm{e}^{+iW_o(\vec{q}')}\} \\
&+ \epsilon(\vec{r}') \otimes \text{IFT}\{\cos[W_e(\vec{q}')]\mathrm{e}^{-iW_o(\vec{q}')}\} \cdot \varphi(\vec{r}') \otimes \text{IFT}\{\sin[W_e(\vec{q}')]\mathrm{e}^{+iW_o(\vec{q}')}\} \\
&+ \epsilon(\vec{r}') \otimes \text{IFT}\{\cos[W_e(\vec{q}')]\mathrm{e}^{-iW_o(\vec{q}')}\} \cdot i\epsilon(\vec{r}') \otimes \text{IFT}\{\sin[W_e(\vec{q}')]\mathrm{e}^{+iW_o(\vec{q}')}\} \\
&+ \epsilon(\vec{r}') \otimes \text{IFT}\{\cos[W_e(\vec{q}')]\mathrm{e}^{-iW_o(\vec{q}')}\} \cdot (-i)\varphi(\vec{r}') \otimes \text{IFT}\{\cos[W_e(\vec{q}')]\mathrm{e}^{+iW_o(\vec{q}')}\} \\
a_3 =\ &+\varphi(\vec{r}') \otimes \text{IFT}\{\sin[W_e(\vec{q}')]\mathrm{e}^{-iW_o(\vec{q}')}\} \\
&+ \varphi(\vec{r}') \otimes \text{IFT}\{\sin[W_e(\vec{q}')]\mathrm{e}^{-iW_o(\vec{q}')}\} \cdot \epsilon(\vec{r}') \otimes \text{IFT}\{\cos[W_e(\vec{q}')]\mathrm{e}^{+iW_o(\vec{q}')}\} \\
&+ \varphi(\vec{r}') \otimes \text{IFT}\{\sin[W_e(\vec{q}')]\mathrm{e}^{-iW_o(\vec{q}')}\} \cdot \varphi(\vec{r}') \otimes \text{IFT}\{\sin[W_e(\vec{q}')]\mathrm{e}^{+iW_o(\vec{q}')}\} \\
&+ \varphi(\vec{r}') \otimes \text{IFT}\{\sin[W_e(\vec{q}')]\mathrm{e}^{-iW_o(\vec{q}')}\} \cdot i\epsilon(\vec{r}') \otimes \text{IFT}\{\sin[W_e(\vec{q}')]\mathrm{e}^{+iW_o(\vec{q}')}\} \\
&+ \varphi(\vec{r}') \otimes \text{IFT}\{\sin[W_e(\vec{q}')]\mathrm{e}^{-iW_o(\vec{q}')}\} \cdot (-i)\varphi(\vec{r}') \otimes \text{IFT}\{\cos[W_e(\vec{q}')]\mathrm{e}^{+iW_o(\vec{q}')}\} \\
a_4 =\ &-i\epsilon(\vec{r}') \otimes \text{IFT}\{\sin[W_e(\vec{q}')]\mathrm{e}^{-iW_o(\vec{q}')}\} \\
&- i\epsilon(\vec{r}') \otimes \text{IFT}\{\sin[W_e(\vec{q}')]\mathrm{e}^{-iW_o(\vec{q}')}\} \cdot \epsilon(\vec{r}') \otimes \text{IFT}\{\cos[W_e(\vec{q}')]\mathrm{e}^{+iW_o(\vec{q}')}\} \\
&- i\epsilon(\vec{r}') \otimes \text{IFT}\{\sin[W_e(\vec{q}')]\mathrm{e}^{-iW_o(\vec{q}')}\} \cdot \varphi(\vec{r}') \otimes \text{IFT}\{\sin[W_e(\vec{q}')]\mathrm{e}^{+iW_o(\vec{q}')}\} \\
&- i\epsilon(\vec{r}') \otimes \text{IFT}\{\sin[W_e(\vec{q}')]\mathrm{e}^{-iW_o(\vec{q}')}\} \cdot i\epsilon(\vec{r}') \otimes \text{IFT}\{\sin[W_e(\vec{q}')]\mathrm{e}^{+iW_o(\vec{q}')}\} \\
&- i\epsilon(\vec{r}') \otimes \text{IFT}\{\sin[W_e(\vec{q}')]\mathrm{e}^{-iW_o(\vec{q}')}\} \cdot (-i)\varphi(\vec{r}') \otimes \text{IFT}\{\cos[W_e(\vec{q}')]\mathrm{e}^{+iW_o(\vec{q}')}\} \\
a_5 =\ &+i\varphi(\vec{r}') \otimes \text{IFT}\{\cos[W_e(\vec{q}')]\mathrm{e}^{-iW_o(\vec{q}')}\} \\
&+ i\varphi(\vec{r}') \otimes \text{IFT}\{\cos[W_e(\vec{q}')]\mathrm{e}^{-iW_o(\vec{q}')}\} \cdot \epsilon(\vec{r}') \otimes \text{IFT}\{\cos[W_e(\vec{q}')]\mathrm{e}^{+iW_o(\vec{q}')}\} \\
&+ i\varphi(\vec{r}') \otimes \text{IFT}\{\cos[W_e(\vec{q}')]\mathrm{e}^{-iW_o(\vec{q}')}\} \cdot \varphi(\vec{r}') \otimes \text{IFT}\{\sin[W_e(\vec{q}')]\mathrm{e}^{+iW_o(\vec{q}')}\} \\
&+ i\varphi(\vec{r}') \otimes \text{IFT}\{\cos[W_e(\vec{q}')]\mathrm{e}^{-iW_o(\vec{q}')}\} \cdot i\epsilon(\vec{r}') \otimes \text{IFT}\{\sin[W_e(\vec{q}')]\mathrm{e}^{+iW_o(\vec{q}')}\} \\
&+ i\varphi(\vec{r}') \otimes \text{IFT}\{\cos[W_e(\vec{q}')]\mathrm{e}^{-iW_o(\vec{q}')}\} \cdot (-i)\varphi(\vec{r}') \otimes \text{IFT}\{\cos[W_e(\vec{q}')]\mathrm{e}^{+iW_o(\vec{q}')}\}
\end{aligned}
\tag{8.9}
$$

In the second iteration, we try to simplify and rearrange the terms. Now we divide the intensity into new four parts:

$$\text{Intensity}(\vec{r}') = b_1(\vec{r}') + b_2(\vec{r}') + b_3(\vec{r}') + b_4(\vec{r}') + b_5(\vec{r}'), \tag{8.10}$$

Terms b_1 - b_5 can be written as:

$$
\begin{aligned}
b_1 =\ & 1 \\
& + \epsilon(\vec{r}') \otimes \text{IFT}\{\cos[W_e(\vec{q}')]\mathrm{e}^{+iW_o(\vec{q}')}\} \\
& + \varphi(\vec{r}') \otimes \text{IFT}\{\sin[W_e(\vec{q}')]\mathrm{e}^{+iW_o(\vec{q}')}\} \\
& + i\epsilon(\vec{r}') \otimes \text{IFT}\{\sin[W_e(\vec{q}')]\mathrm{e}^{+iW_o(\vec{q}')}\} \\
& - i\varphi(\vec{r}') \otimes \text{IFT}\{\cos[W_e(\vec{q}')]\mathrm{e}^{+iW_o(\vec{q}')}\} \\
& + \epsilon(\vec{r}') \otimes \text{IFT}\{\cos[W_e(\vec{q}')]\mathrm{e}^{-iW_o(\vec{q}')}\} \\
& + \varphi(\vec{r}') \otimes \text{IFT}\{\sin[W_e(\vec{q}')]\mathrm{e}^{-iW_o(\vec{q}')}\} \\
& - i\epsilon(\vec{r}') \otimes \text{IFT}\{\sin[W_e(\vec{q}')]\mathrm{e}^{-iW_o(\vec{q}')}\} \\
& + i\varphi(\vec{r}') \otimes \text{IFT}\{\cos[W_e(\vec{q}')]\mathrm{e}^{-iW_o(\vec{q}')}\} \\
b_2 =\ & +\epsilon(\vec{r}') \otimes \text{IFT}\{\cos[W_e(\vec{q}')]\mathrm{e}^{-iW_o(\vec{q}')}\} \cdot \epsilon(\vec{r}') \otimes \text{IFT}\{\cos[W_e(\vec{q}')]\mathrm{e}^{+iW_o(\vec{q}')}\} \\
& + \epsilon(\vec{r}') \otimes \text{IFT}\{\cos[W_e(\vec{q}')]\mathrm{e}^{-iW_o(\vec{q}')}\} \cdot \varphi(\vec{r}') \otimes \text{IFT}\{\sin[W_e(\vec{q}')]\mathrm{e}^{+iW_o(\vec{q}')}\} \\
& + \epsilon(\vec{r}') \otimes \text{IFT}\{\cos[W_e(\vec{q}')]\mathrm{e}^{-iW_o(\vec{q}')}\} \cdot i\epsilon(\vec{r}') \otimes \text{IFT}\{\sin[W_e(\vec{q}')]\mathrm{e}^{+iW_o(\vec{q}')}\} \\
& + \epsilon(\vec{r}') \otimes \text{IFT}\{\cos[W_e(\vec{q}')]\mathrm{e}^{-iW_o(\vec{q}')}\} \cdot (-i)\varphi(\vec{r}') \otimes \text{IFT}\{\cos[W_e(\vec{q}')]\mathrm{e}^{+iW_o(\vec{q}')}\} \quad (8.11) \\
b_3 =\ & +\varphi(\vec{r}') \otimes \text{IFT}\{\sin[W_e(\vec{q}')]\mathrm{e}^{-iW_o(\vec{q}')}\} \cdot \epsilon(\vec{r}') \otimes \text{IFT}\{\cos[W_e(\vec{q}')]\mathrm{e}^{+iW_o(\vec{q}')}\} \\
& + \varphi(\vec{r}') \otimes \text{IFT}\{\sin[W_e(\vec{q}')]\mathrm{e}^{-iW_o(\vec{q}')}\} \cdot \varphi(\vec{r}') \otimes \text{IFT}\{\sin[W_e(\vec{q}')]\mathrm{e}^{+iW_o(\vec{q}')}\} \\
& + \varphi(\vec{r}') \otimes \text{IFT}\{\sin[W_e(\vec{q}')]\mathrm{e}^{-iW_o(\vec{q}')}\} \cdot i\epsilon(\vec{r}') \otimes \text{IFT}\{\sin[W_e(\vec{q}')]\mathrm{e}^{+iW_o(\vec{q}')}\} \\
& + \varphi(\vec{r}') \otimes \text{IFT}\{\sin[W_e(\vec{q}')]\mathrm{e}^{-iW_o(\vec{q}')}\} \cdot (-i)\varphi(\vec{r}') \otimes \text{IFT}\{\cos[W_e(\vec{q}')]\mathrm{e}^{+iW_o(\vec{q}')}\} \\
b_4 =\ & -i\epsilon(\vec{r}') \otimes \text{IFT}\{\sin[W_e(\vec{q}')]\mathrm{e}^{-iW_o(\vec{q}')}\} \cdot \epsilon(\vec{r}') \otimes \text{IFT}\{\cos[W_e(\vec{q}')]\mathrm{e}^{+iW_o(\vec{q}')}\} \\
& - i\epsilon(\vec{r}') \otimes \text{IFT}\{\sin[W_e(\vec{q}')]\mathrm{e}^{-iW_o(\vec{q}')}\} \cdot \varphi(\vec{r}') \otimes \text{IFT}\{\sin[W_e(\vec{q}')]\mathrm{e}^{+iW_o(\vec{q}')}\} \\
& - i\epsilon(\vec{r}') \otimes \text{IFT}\{\sin[W_e(\vec{q}')]\mathrm{e}^{-iW_o(\vec{q}')}\} \cdot i\epsilon(\vec{r}') \otimes \text{IFT}\{\sin[W_e(\vec{q}')]\mathrm{e}^{+iW_o(\vec{q}')}\} \\
& - i\epsilon(\vec{r}') \otimes \text{IFT}\{\sin[W_e(\vec{q}')]\mathrm{e}^{-iW_o(\vec{q}')}\} \cdot (-i)\varphi(\vec{r}') \otimes \text{IFT}\{\cos[W_e(\vec{q}')]\mathrm{e}^{+iW_o(\vec{q}')}\} \\
b_5 =\ & +i\varphi(\vec{r}') \otimes \text{IFT}\{\cos[W_e(\vec{q}')]\mathrm{e}^{-iW_o(\vec{q}')}\} \cdot \epsilon(\vec{r}') \otimes \text{IFT}\{\cos[W_e(\vec{q}')]\mathrm{e}^{+iW_o(\vec{q}')}\} \\
& + i\varphi(\vec{r}') \otimes \text{IFT}\{\cos[W_e(\vec{q}')]\mathrm{e}^{-iW_o(\vec{q}')}\} \cdot \varphi(\vec{r}') \otimes \text{IFT}\{\sin[W_e(\vec{q}')]\mathrm{e}^{+iW_o(\vec{q}')}\} \\
& + i\varphi(\vec{r}') \otimes \text{IFT}\{\cos[W_e(\vec{q}')]\mathrm{e}^{-iW_o(\vec{q}')}\} \cdot i\epsilon(\vec{r}') \otimes \text{IFT}\{\sin[W_e(\vec{q}')]\mathrm{e}^{+iW_o(\vec{q}')}\} \\
& + i\varphi(\vec{r}') \otimes \text{IFT}\{\cos[W_e(\vec{q}')]\mathrm{e}^{-iW_o(\vec{q}')}\} \cdot (-i)\varphi(\vec{r}') \otimes \text{IFT}\{\cos[W_e(\vec{q}')]\mathrm{e}^{+iW_o(\vec{q}')}\},
\end{aligned}
$$

where the linear terms are described in b_1.

After this expansion of the individual terms, it is convenient to convert these terms into reciprocal space, in which the $E(\vec{q'})$ and $\Phi(\vec{q'})$ functions are then found.

$$\text{Intensity}(\vec{q}) = c_1(\vec{q}) + c_2(\vec{q}) + c_3(\vec{q}) + c_4(\vec{q}) + c_5(\vec{q}) \tag{8.12}$$

Using the Eq. 8.3, the Fourier transform of terms b_1 - b_5 is calculated as:

$$\text{FT}\{\epsilon(\vec{r'}) \otimes \text{IFT}\{\cos[W_e(\vec{q'})]\mathrm{e}^{+\mathrm{i}W_o(\vec{q'})}\}\} = E(\vec{q'})\cos[W_e(\vec{q'})]\mathrm{e}^{+\mathrm{i}W_o(\vec{q'})}, \tag{8.13}$$

where the second term in expression b_1 was used as an example.

These terms in the reciprocal space can be written as:

$$
\begin{aligned}
c_1 = {}& \delta(\vec{q'})+ \\
& + E(\vec{q'})\cos[W_e(\vec{q'})]\mathrm{e}^{+\mathrm{i}W_o(\vec{q'})} \\
& + \Phi(\vec{q'})\sin[W_e(\vec{q'})]\mathrm{e}^{+\mathrm{i}W_o(\vec{q'})} \\
& + \mathrm{i}E(\vec{q'})\sin[W_e(\vec{q'})]\mathrm{e}^{+\mathrm{i}W_o(\vec{q'})} \\
& - \mathrm{i}\Phi(\vec{q'})\cos[W_e(\vec{q'})]\mathrm{e}^{+\mathrm{i}W_o(\vec{q'})} \\
& + E(\vec{q'})\cos[W_e(\vec{q'})]\mathrm{e}^{-\mathrm{i}W_o(\vec{q'})} \\
& + \Phi(\vec{q'})\sin[W_e(\vec{q'})]\mathrm{e}^{-\mathrm{i}W_o(\vec{q'})} \\
& - \mathrm{i}E(\vec{q'})\sin[W_e(\vec{q'})]\mathrm{e}^{-\mathrm{i}W_o(\vec{q'})} \\
& + \mathrm{i}\Phi(\vec{q'})\cos[W_e(\vec{q'})]\mathrm{e}^{-\mathrm{i}W_o(\vec{q'})} \\
c_2 = {}& +E(\vec{q'})\cos[W_e(\vec{q'})]\mathrm{e}^{-\mathrm{i}W_o(\vec{q'})}\otimes \\
& \{E(\vec{q'})\cos[W_e(\vec{q'})]\mathrm{e}^{+\mathrm{i}W_o(\vec{q'})} + \Phi(\vec{q'})\sin[W_e(\vec{q'})]\mathrm{e}^{+\mathrm{i}W_o(\vec{q'})} \\
& + \mathrm{i}(\vec{q'})\sin[W_e(\vec{q'})]\mathrm{e}^{+\mathrm{i}W_o(\vec{q'})} - \mathrm{i}\Phi(\vec{q'})\cos[W_e(\vec{q'})]\mathrm{e}^{+\mathrm{i}W_o(\vec{q'})}\} \\
c_3 = {}& +\Phi(\vec{q'})\sin[W_e(\vec{q'})]\mathrm{e}^{-\mathrm{i}W_o(\vec{q'})}\otimes \\
& \{E(\vec{q'})\cos[W_e(\vec{q'})]\mathrm{e}^{+\mathrm{i}W_o(\vec{q'})} + \Phi(\vec{q'})\text{IFT}\sin[W_e(\vec{q'})]\mathrm{e}^{+\mathrm{i}W_o(\vec{q'})} \\
& + \mathrm{i}E(\vec{q'})\sin[W_e(\vec{q'})]\mathrm{e}^{+\mathrm{i}W_o(\vec{q'})}\} - \mathrm{i}\Phi(\vec{q'})\cos[W_e(\vec{q'})]\mathrm{e}^{+\mathrm{i}W_o(\vec{q'})}\} \\
c_4 = {}& -\mathrm{i}E(\vec{q'})\sin[W_e(\vec{q'})]\mathrm{e}^{-\mathrm{i}W_o(\vec{q'})}\otimes \\
& \{E(\vec{q'})\cos[W_e(\vec{q'})]\mathrm{e}^{+\mathrm{i}W_o(\vec{q'})} + \Phi(\vec{q'})\sin[W_e(\vec{q'})]\mathrm{e}^{+\mathrm{i}W_o(\vec{q'})} \\
& + \mathrm{i}E(\vec{q'})\sin[W_e(\vec{q'})]\mathrm{e}^{+\mathrm{i}W_o(\vec{q'})} - \mathrm{i}\Phi(\vec{q'})\text{IFT}\cos[W_e(\vec{q'})]\mathrm{e}^{+\mathrm{i}W_o(\vec{q'})}\} \\
c_5 = {}& +\mathrm{i}\Phi(\vec{q'})\cos[W_e(\vec{q'})]\mathrm{e}^{-\mathrm{i}W_o(\vec{q'})}\otimes \\
& \{E(\vec{q'})\cos[W_e(\vec{q'})]\mathrm{e}^{+\mathrm{i}W_o(\vec{q'})} + \Phi(\vec{q'})\sin[W_e(\vec{q'})]\mathrm{e}^{+\mathrm{i}W_o(\vec{q'})} \\
& + \mathrm{i}E(\vec{q'})\sin[W_e(\vec{q'})]\mathrm{e}^{+\mathrm{i}W_o(\vec{q'})} - \mathrm{i}\Phi(\vec{q'})\cos[W_e(\vec{q'})]\mathrm{e}^{+\mathrm{i}W_o(\vec{q'})}\}.
\end{aligned}
\tag{8.14}
$$

Term c_1 represents the linear terms in the intensity while terms c_2 - c_5 are the addition of non-linear terms.

9. List of Abbreviations

ADU	Analog-to-digital
CTF	Contrast transfer function
CFEG	Cold field emission gun
CF	Conversion factor
$\otimes$	Convolution
CryoEM	Cryo-electron microscopy
$C_{1,0}$	Defocus
$C_{3,0}$	Spherical aberration
DQE	Detection quantum efficiency
$E(\vec{q})$	Amplitude object function
EM	Electron microscopy
$\mathbf{E}$	Envelope function
E_d	Sample drift envelope
E_s	Spatial envelope
E_t	Temporal envelope
E_u	Specimen vibration envelope
FT	Fourier transform
IFT	Inverse Fourier transform
Φ_e	Incident electron flux
I_dc	Dark current
I_rn	Readout noise
MTF	Modulation spread function
NTF	Noise transfer function
$\mathcal{N}$	Normalised noise power spectrum
$\Phi(\vec{q})$	Phase object function
PSF	Point spread function
P_oiss	Poisson noise yield

STEM	Scanning transmission electron microscopy
SFEG	Schottky field emission gun
S/N	Singal-to-noise ratio
SPA	Single particle analysis
TEM	Transmission electron microscopy
W	Aberration polynomial
W_e	Even order aberrations
W_o	Odd order aberrations